Article:

Keylock, C.J., Constantinescu, G. and Hardy, R.J. (2012) The application of computational fluid dynamics to natural river channels: Eddy resolving versus mean flow approaches. Geomorphology, 179. 1 - 20. ISSN 0169-555X

https://doi.org/10.1016/j.geomorph.2012.09.006

Published paper

Keylock, C.J., Constantinescu, G. and Hardy, R.J. (2012) *The application of computational fluid dynamics to natural river channels: Eddy resolving versus mean flow approaches.* Geomorphology, 179. 1 - 20. ISSN 0169-555X
http://dx.doi.org/10.1016/j.geomorph.2012.09.006

The application of computational fluid dynamics to natural river channels: Eddy resolving versus mean flow approaches

Keylock C. J[1*], Constantinescu, G.[2], Hardy, R. J.[3]

[1] Department of Civil and Structural Engineering, Sir Fredrick Mappin Building, Mappin Street, University of Sheffield, Sheffield, S1 3JD, U.K.

e-mail: c.keylock@sheffield.ac.uk, tel: 0114 222 5705, fax 0114 222 5700

[2] Civil & Environmental Engineering Department, IIHR-Hydroscience and Engineering, The University of Iowa, Stanley Hydraulics Laboratory, Iowa City, IA 52242

[3] Department of Geography, Durham University, Science Laboratories, South Road, Durham, DH1 3LE, UK

*Corresponding author

Abstract

In the last decade, as computing power has increased, there has been an explosion in the use of eddy-resolving numerical methods in the engineering, earth and environmental sciences. For complex geomorphic flows, where accurate field investigations are difficult to perform and where experiments may be difficult to scale, these numerical approaches are beginning to give key insights into the nature of these flows. Eddy-resolving methods such as Large and Detached Eddy Simulation (LES/DES) may be contrasted with the time-averaged, three-dimensional simulations that only really began to be applied seriously in geomorphology fifteen years ago. While the potential of LES for geomorphology has been examined previously, DES is a relatively recent method that deserves further consideration. In this paper, we explain the method and then utilise examples from meander and confluence flows, as well as flow near the bed of a gravel bed river, to highlight the improvements to both the representation of the mean flow, and to the

representation of time-varying processes, that result from the use of LES/DES. Some suggestions are provided for the future use of such techniques in geomorphology.

Keywords: Large eddy simulation; Detached eddy simulation; Meanders; Confluences; Gravel-bed rivers; Sediment transport

1. Introduction

It is now over a decade since Lane et al. (1999) demonstrated the advantages to fluvial geomorphology in moving from modelling tools based on the shallow water equations to computational fluid dynamics (CFD) approaches that resolve both the vertical component of velocity and the pressure field. One only needs to consider a common occurrence in nature, the flow in a gently curved channel such as a meander bend, to see the advantages gained from modelling using CFD. Because flow velocities increase away from the bed and centripetal forces are proportional to the velocity squared, the upper part of the flow is preferentially deflected towards the outer part of the bend. Thus, a counter-directional flow is established near the bed. A depth-averaged flow model would incorporate topographically-based friction terms to account for the losses associated with curvature-induced secondary flow, and the mean flow would be correctly directed towards the outer bank. However, if as a geomorphologist or as a river manager one is interested in bedload sediment transport (Julien and Anthony, 2002; Clayton and Pitlick, 2007), or the effect on hyporheic zone flow and ecology (Brunke and Gonser, 1997; Tonina and Buffington, 2011; Boano et al., 2011), these mean vectors are not necessarily aligned with the near-wall flow, implying that shallow water models are of limited utility for gaining an understanding of such phenomena. Of course, in steeper meander bends, where flow separation and shearing between the main flow and recirculating flow takes place (Ferguson et al., 2003), issues concerning the representation of flow processes are exacerbated.

Lane et al. (1999) considered the mean flow approach to CFD, also known as Reynolds Averaged Navier-Stokes or RANS modelling. However, since that work, there has been an increased use of eddy-resolving modelling techniques both in fluvial geomorphology and in fluids engineering more generally, which permit the time-varying flow field to be resolved. Given that under the majority of flow conditions experienced annually, bedload transport will be driven by peaks in turbulence stresses exerted by flow structures (the mean flow exerts a subcritical shear stress) and, given the importance of shear phenomena in many fluvial flows including steep meanders, confluences (Best and Roy, 1991; Biron et al., 1993) and flow about individual large clasts (Buffin-Bélanger and Roy, 1998; Lawless and Robert, 2001), a much more realistic description of the flow is possible with such modelling techniques. As an example, consider the flow over a step, which is a simple analogue for flow over a transition in bed elevation. The adverse pressure gradient results in flow separation at the top of the step. The flow reattaches at about 6 to 7 step heights downstream of the step (Simpson, 1989) and between the step and this point the mean flow is upstream, resulting in the development of a shear layer between the upper and lower flows. Based on the mean flow, the place where we would least expect bedload entrainment is at the reattachment point where the mean velocity in the downstream component is zero. However, it is at this point where the shear layer impinges on the wall meaning that turbulent stresses are high and, in fact, sediment entrainment is close to maximal. Hence, it is clear that in complex natural channels, turbulence must be modelled correctly for capturing mixing processes that affect pollutant dispersal, or the turbulent phenomena that affect sediment entrainment and deposition.

Eddy-resolving methods are computationally expensive, which explains why, in an early review of large-eddy simulation's applicability to fluvial geomorphology, Keylock et al. (2005) concluded that, even with the use of wall functions to minimise the computational expense of resolving flow close to the bed, the use of such modelling methods to (multi)reach scale processes would be limited for the foreseeable future. Hence, such techniques are primarily of interest for studying laboratory experiments of flow in channels (Hardy et al., 2007, 2009) and/or channels containing structures such as groynes (McCoy et al., 2008) or spur dikes (Koken and Constantinescu 2008a,b). However, in the last ten years the engineering literature has seen an explosion in the use of hybrid RANS-LES methods that permit the largest flow structures to be resolved without the computational cost of well-resolved (no wall functions) large-eddy simulations. Thus, with the loss of resolution of smaller scale-flow structures, it is possible to extend the computational domain within a formally correct modelling framework that switches eddy resolving on or off depending on local flow conditions and level of mesh refinement. Such methods have great potential within fluvial geomorphology and the aim of this paper is to describe the basis of such techniques and to demonstrate how eddy-resolving methods add significantly to our understanding of geomorphic flows. In particular we focus on one variant of the hybrid methods called Detached Eddy Simulation (DES) (Spalart and Allmaras, 1994), which is by far the most popular owing to its demonstrated accuracy in high Reynolds number, wall-bounded, complex turbulent flows. We also briefly review large-eddy simulation methods although Keylock et al. (2005) provided a more detailed treatment of this method.

2. The fundamental equations and RANS and LES approximations

2.1 Introduction

A detailed coverage of the essentials is available from a range of sources. As they relate to geomorphology, the reader is recommended to look at Bates et al. (2005) for a discussion of the Navier-Stokes equations and RANS methods, while Keylock et al. (2005) explained the derivation of the LES equations and also discussed a number of the methods used to approximate the behaviour of the small scales in such flows. More generally, in fluid mechanics, Sagaut (2005) and Geurts (2003) provide a thorough discussion of LES methods.

2.2 The Navier-Stokes equations and closure

Whether or not one is using DES, LES or RANS, because one is approximating the full complexity of the Navier-Stokes equations, it is necessary to introduce a term to the primary equations to close off the effects of making this approximation (the closure problem). Because this closure term is formulated beyond the immediate frame of reference of the other terms in the equation, one then needs to write a model for this closure term. With (steady) RANS, the closure term originates from time-varying behaviour of the flow as the model equations are written in terms of time-averaged velocities. For LES, the problem is to model the scales of the flow that are not resolved explicitly as they are smaller than the filter that we apply to the Navier-Stokes equations. DES tries to model the energetically important eddies in regions where the mesh resolution is sufficient to permit this.

To formalise this somewhat, we first write down the Navier-Stokes equations, before stating the Reynolds averaging procedure used in RANS and the spatial filtering used in LES. From this, the respective approximations to the Navier-Stokes momentum equations may be compared. The conservation of mass or continuity equation for the incompressible Navier-Stokes equations is given by

$$\frac{\partial u}{\partial x}+\frac{\partial v}{\partial y}+\frac{\partial w}{\partial z}\equiv\frac{\partial u_1}{\partial x_1}+\frac{\partial u_2}{\partial x_2}+\frac{\partial u_3}{\partial x_3}\equiv\frac{\partial u_i}{\partial x_i}=0 \tag{1}$$

where the notation on the far left-hand side provides unique identifiers to each velocity component (*u, v, w*) and coordinate (*x, y ,z*), but thereafter, $i\in\{1,2,3\}$ and u_1 is the longitudinal velocity component, u_2 is the transverse component and u_3 is the vertical velocity, and *x* indicates a spatial coordinate. Because of the need to consider more than one component at a time, in the equations below, the index *j* is also used to represent different spatial coordinates. The Navier-Stokes momentum equations may be written in the following concise manner, which is equivalent in form to the Einstein summation notation used on the right-most version of the left-hand side of (1):

$$\frac{\partial u_i}{\partial t}+\frac{\partial (u_i u_j)}{\partial x_j}=-\frac{1}{\rho}\frac{\partial p}{\partial x_i}+\frac{\partial}{\partial x_j}\left[\nu\left(\frac{\partial u_i}{\partial x_j}+\frac{\partial u_j}{\partial x_i}\right)\right] \tag{2}$$

where *t* is time, *p* is pressure and viscosity, *v*, is in the kinematic form. Hence, equation (2) is actually a set of three coupled equations, each considering the time derivative of a different component in the left-hand term. The Reynolds decomposition separates a velocity into its temporal mean (overbar) and fluctuating (prime) components according to:

$$u_i = \overline{u_i} + u_i' \tag{3}$$

If we are time-averaging (2) using (3), we obtain:

$$\overline{u}_j \frac{\partial \overline{u}_i}{\partial x_j} = -\frac{1}{\rho}\frac{\partial \overline{p}}{\partial x_j} + \frac{\partial}{\partial x_j}\left[\nu\left(\frac{\partial \overline{u}_i}{\partial x_j} + \frac{\partial \overline{u}_j}{\partial x_i}\right) - \rho\overline{u_i' u_j'}\right] \tag{4}$$

where the closure term on the right-hand side reflects the effect of the fluctuating velocities on the mean flow and is termed the Reynolds stress tensor. Hence, from the RANS perspective, turbulence has an effect on the mean flow that must be accounted for, but this can be done solely through the velocity covariance. Nonlinear relations between velocity components, or phenomena such as coherent structures are not relevant from the RANS perspective. There are a number of strategies for closing (4) by writing a model for how turbulence behaves (e.g. Speziale, 1987). However, the classic model is that due to Launder et al. (1975) who wrote a two-equation model for the transport of turbulent kinetic energy and turbulence dissipation, from which the Reynolds stresses could be derived.

2.3 Large eddy simulation

The LES equations are derived by applying a spatial filtering operation to the velocity, rather than a temporal averaging. Hence, we obtain a decomposition:

$$u_i = \tilde{u}_i + u_i'' \tag{5}$$

where ~ indicates the velocity over the spatial scales greater than the size of the filter and the double prime indicates the sub-filter scales. We filter the equations using a convolution operation and classically, one chooses a simple top-hat filter, although there are various possibilities here that are formally correct (Vreman et al., 1994). In n dimensions, for an arbitrary direction, x, a top hat filter of width, Δ, positioned at x^+ equals $1 / \Delta^n$ for $|x - x^+| \leq \Delta$ and takes a value of 0 for $|x - x^+| > \Delta$. Traditionally, the filter width was made the same size as the computational mesh, meaning that the resulting scales were referred to as grid scales and subgrid-scales. However, it is also possible to decouple the filtering operations from the mesh size employed. Substitution of (5) into (2) gives the LES momentum equation:

$$\frac{\partial \tilde{u}_i}{\partial t} + \frac{\partial(\tilde{u}_i \tilde{u}_j)}{\partial x_j} = -\frac{1}{\rho}\frac{\partial \tilde{p}}{\partial x_i} + \frac{\partial}{\partial x_j}\left[\nu\left(\frac{\partial \tilde{u}_i}{\partial x_j} + \frac{\partial \tilde{u}_j}{\partial x_i}\right) - \tau_{ij}^{SFS}\right] \tag{6}$$

where the subfilter scale stress tensor, τ_{ij}^{SFS}, may be decomposed into

$$\tau_{ij}^{SFS} = \left(\widetilde{\tilde{u}_i \tilde{u}_j} - \tilde{u}_i \tilde{u}_j\right) + \left(\widetilde{\tilde{u}_i u_j^{//}} + \widetilde{\tilde{u}_j u_i^{//}}\right) + \widetilde{u_i^{//} u_j^{//}} \tag{7}$$

where the right-hand term is the filtered analogy of the Reynolds stress. The standard model for the subfilter-scale stresses is the eddy viscosity model of Smagorinsky (1963). The basic idea for an eddy viscosity model is due to Boussinesq (1877) who reasoned that the turbulence fluctuations represented by the Reynolds stresses, would act on the mean flow in a similar manner to viscous forces. Thus, the Reynolds stresses could be equated to mean deformation rates:

$$\tau_{ij} = -\rho \overline{u_i^{/} u_j^{/}} = \mu_t \left(\frac{\partial U_j}{\partial x_i} + \frac{\partial U_i}{\partial x_j}\right) \tag{8}$$

The eddy viscosity approach is also termed a mixing length model, because, from dimensional analysis, if we divide through by the density, the dynamic viscosity, μ_t, becomes a kinematic viscosity, ν_t, with dimensions of length-squared per unit time and, thus, composed of the product of a length scale, ℓ, a velocity scale, Υ, and a constant of proportionality, c_1. Given a mean velocity gradient (and we consider this always to be positive by looking at the absolute part) of $\left|\frac{\partial U_i}{\partial x_j}\right|$, the velocity scale should be:

$$\Upsilon = c_2 \ell \left|\frac{\partial U_i}{\partial x_j}\right| \tag{9}$$

Hence, absorbing c_1 and c_2 into a modified length scale, ℓ_m, we may write the kinematic viscosity as:

$$\nu_t = \ell_m^2 \left|\frac{\partial U_i}{\partial x_j}\right| \tag{10}$$

Not only can this type of model be used to model the Reynolds stresses in (4), but its direct analogy can be used in LES to determine the right-hand term in (7). In this case, the mixing length scale is equated to the product of the length of the filter and a constant, termed the Smagorinsky constant, with a typical value of about 0.1, although choice varies with the type of flow considered.

2.4 Dynamic LES methods

It is generally the case that this method can be improved upon by permitting the coefficient to vary dynamically with the local properties of the flow. This is done by using a test filter at some larger scale than the actual filter scale to feed information to the filter scale on larger scale deformation rates. The Smagorinsky model and this dynamic procedure are discussed in more detail by Keylock et al. (2005, p.280-281) and are adopted below in our examples. The description provided here of RANS and Smagorinsky-type subfilter-scale modelling is useful for understanding the basis for the detached eddy simulation method (DES). It should be noted that high resolution LES studies resolve the flow all the way towards the boundary surfaces, including the viscous sub-layer. However, one way to speed up the performance of LES is to use wall functions to bridge the distance from surfaces to the centre of the first computational cell situated outside the viscous sub-layer (Piomelli and Balaras, 2002; Wang and Moin, 2002). It is computationally much less expensive to impose a function over this distance than to employ smaller and smaller cells near these surfaces to resolve the required flow and turbulence fields. This strategy is used in many geomorphic studies but, as shown by Constantinescu et al. (2011a) and discussed below, DES can be more accurate than LES with wall functions. In fact, one can think of DES as LES with a more sophisticated wall model.

Because LES retains the time derivative in the solutions a time series of velocities for each grid cell at the input to the flow domain needs to be specified (in addition, to the standard boundary conditions for the walls, outlet and free surface required in RANS applications). The exact nature of the inlet conditions will have some effect on the resolved flow field (Aider et al., 2007) and a range of methods for deriving inlet generation conditions have been proposed (see the review by Tabor and Baba-Ahmadi, 2010). The conclusion from our work in this area would suggest that for sediment entrainment, or vortex-induced scour where the flow conditions at the front face of an obstacle that breaks up the boundary layer are important, a sophisticated inlet condition generation scheme is necessary. This is also the case for flows without significant mixing or shear, where the effect of the inlet condition lasts a long way into the numerical domain. However, in a wake region, the intense mixing means that upstream effects are soon lost. Hence, simpler inlet conditions that preserve the relevant individual velocities and Fourier spectra, but not necessarily any cross-spectral or nonlinear information, are sufficient (Keylock et al., 2011).

3. Detached Eddy Simulation

Detached eddy simulation provides a means of switching between RANS and LES depending on the local flow state, meaning that eddies are resolved where vortex dynamics are deemed to be important but are suppressed elsewhere, leading to less time-consuming calculations. Because DES reduces to a fairly complex RANS model near solid surfaces, the method is in some ways less *ad hoc* than combining wall functions with LES. This is because the latter approach automatically assumes the existence of a logarithmic region in the vicinity of the surface, an assumption that is well known to break down in flows containing regions of strong pressure gradients and separation. However, DES is restricted to closures that are specific solutions to the general closure equation employed. This is due to Spalart and Allmaras (1994) and, in essence, represents turbulence by its effect on viscosity (an eddy-viscosity model similar to the Smagorinsky model).

The Spalart-Allmaras model is based on earlier work by Baldwin and Barth (1991). We begin by defining an adjusted, kinematic, turbulent eddy viscosity as:

$$\nu_t = \frac{\mu_t}{\rho\left[\frac{(\nu_t/\nu)^3}{(\nu_t/\nu)^3 + c_{v1}^3}\right]} \tag{11a}$$

where μ_t is the dynamic, turbulent eddy viscosity, v is the molecular, kinematic viscosity, ρ is the fluid density and c_{v1} = 7.1 is a constant used to scale the kinematic viscosity appropriately all the way to the boundary, hence, its value reflects experimental data on the scaling of the log layer and buffer layers. To simplify notation in what follows, we write:

$$\nu_t = \frac{\mu_t}{\rho f_{v1}}$$

$$f_{v1} = \frac{\chi^3}{\chi^3 + c_{v1}^3}$$

$$\chi = \frac{\nu_t}{\nu} \tag{11b}$$

An equation is then written for the total derivative of v_t from which results may be derived in terms of μ_t using (8). This is based on balancing the production and destruction of v_t. The original model also included a term that would "trip" a laminar region into a turbulent response as a function of the velocity difference near the wall. However, as is the case of the majority of applications of the method, here we assume that the flow is fully turbulent and that this term may be neglected. Production is a function of the magnitude of the vorticity, which establishes a difference with two-equation RANS models that are based on strain rates. Destruction was based on distance from surfaces, *d*, on the basis that the confinement of the spatial extent of eddies by the pressure will be a function of *d*. The full, one equation model is:

$$\frac{\partial \nu_t}{\partial t} + u_i \frac{\partial \nu_t}{\partial x_i} = c_{b1}(1 - f_{t2})\check{S}\nu_t - \left[c_{w1} f_w - \frac{c_{b1}}{\kappa^2} f_{t2}\right]\left(\frac{\nu_t}{d}\right)^2 + \frac{1}{\varsigma}\left[\frac{\partial}{\partial x_i}\left((\nu + \nu_t)\frac{\partial \nu_t}{\partial x_i}\right) + c_{b2}\left(\frac{\partial \nu_t}{\partial x_j}\right)^2\right] \quad (12)$$

where Einstein summation notation is used as adopted earlier in this paper. If $S = \sqrt{2\omega_{ij}\omega_{ij}}$ is the magnitude of the vorticity, and $\omega_{ij} = \frac{1}{2}\left(\frac{\partial u_i}{\partial x_j} - \frac{\partial u_j}{\partial x_i}\right)$, then

$$\check{S} = S + \frac{\nu_t}{\kappa^2 d^2} f_{v2} \quad (13)$$

where $f_{v2} = 1 - \frac{\chi}{1 + \chi f_{v1}}$ and $f_{t2} = c_{t3}\exp(-c_{t4}\chi^2)$. The final function in (12) to define is

$$f_w = h\left[\frac{1 + c_{w3}^6}{h^6 + c_{w3}^6}\right]^{1/6} \quad (14)$$

where $h = r + c_{w2}(r^6 - r)$, and $r = \nu_t / \check{S}\kappa^2 d^2$.

Values for all the model coefficients are given in Table 1. Detached eddy simulation replaces the distance to the wall, *d*, with the modified distance function: $\check{d} \equiv \min\{d, c_{DES}\Delta\}$, where *Δ* is the maximum dimension of the computational mesh and c_{DES} is a coefficient taken to be 0.65 based on simulations of forced isotropic turbulence. Hence, near the wall, the model operates in RANS mode based on the distance, *d*. Further from the wall, the length scale $c_{DES}\Delta$ means that in regions where the production and destruction terms in (12) are in balance, $\nu_t \propto S\Delta^2$, which, given the assumption in DES concerning the approximation of strain rates by vorticity, yields a form similar to the

Smagorinsky model, described in Section 2. In terms of practical implementation of this method, it is important to ensure that $\tilde{S}$ does not reach zero during calculations to prevent numerical instability. The simplest way to do this is to clip values at some value greater than zero. It is also important to note that the f_{t2} term in the model originated from a correction needed for the "trip" term. If the latter is excluded then it is perfectly logical to exclude f_{t2} as well (Aupoix and Spalart, 2003). This does not appear to have a major effect on the results at high Reynolds numbers (Rumsey, 2007).

Table 1. Coefficients in the Spalart and Allmaras (1994) model.

Coefficient	Value	Coefficient	Value
c_{v1}	7.1	c_{w2}	0.3
c_{b1}	0.1355	c_{w3}	2.0
c_{t3}	1.2	c_{b2}	0.622
c_{t4}	0.5	K	0.41
c_{w1}	$\frac{c_{b1}}{\kappa^2} + \frac{1 + c_{b2}}{\xi}$	Σ	2/3

The Spalart-Allmaras one equation model is not based on such firm theoretical foundations as the two-equation models for turbulence production and dissipation used in RANS. However, RANS modellers often make use of one-equation models today as their accuracy is still good. When the LES mode is active, the form of this DES model approximately reduces to an eddy-viscosity like Smagorinsky model. However, because (9) includes transport and history effects, there is an attempt to reproduce the behaviour of dynamic filtering methods (Germano, 1992; Porté-Agel et al., 2000). However, alternative subfilter scale schemes (Geurts and Holm, 2003) cannot be implemented. One should also note that DES formulations based on two-equation RANS models (e.g., k-ω SST) are now available, though the Spalart-Allmaras version remains by far the most popular (e.g., see Chang et al., 2007).

Detached Eddy Simulation is currently used extensively and a comparison of its performance to well-resolved LES and RANS methods is given by Spalart (2000). An example comparing DES for flow over a sphere at various Reynolds numbers is given by Constantinescu and Squires (2004). Computation using well-resolved LES at the highest Reynolds numbers past the drag crisis would have been very costly and the authors were able to conclude that DES was able to predict the mean drag coefficient to an accuracy compatible with experiments at the same Reynolds number (Re ~10^6). In addition, eddy-shedding was observed that consisted of high frequency shedding of individual vortices within the shear layers and lower frequency flapping of the shear layer.

4. Application of eddy-resolving numerical methods to geomorphic flows

This section of the paper discusses the application of eddy resolving methods in a variety of geomorphic contexts and at different scales. In each case, the simulations fulfil the guidelines for mesh resolution that we articulate in section 6. Flows through meander and confluences where focus is on structure much larger than a bedload grain size are considered initially, before looking at near-wall flow where the scale of turbulent structures is smaller. The section finishes by considering sediment entrainment and transport from the perspective of eddy resolving simulations.

4.1 Meanders

Most natural rivers contain meandering regions. To a large extent, their morphodynamics is controlled by erosion at the bed and outer bank due to redistribution of the streamwise momentum primarily by curvature-induced secondary flow within and downstream of the high-curvature reaches. In the case of alluvial open channels, the main cell of cross stream circulation occupies the deeper part of the section. However, in regions where the bed is fairly flat, the main cell can extend over most of the cross section (Blanckaert, 2010). Depending on the flow conditions, bathymetry and channel curvature, besides the main cell of cross stream circulation, several other streamwise oriented vortical (SOV) cells can form close to the outer and inner banks of the reach. The presence of SOV cells and the associated cross-stream circulation play an important role in the transport of sediment, contaminant and heat within rivers. When the cores of these cells are situated close to loose boundaries, they can induce severe local erosion. In curved reaches, the core of high streamwise velocities shifts gradually from the inner bank toward the outer bank under the influence of the transverse pressure gradients and secondary cross flow. Since the main cell of cross-stream circulation persists some distance downstream of the region of high channel curvature, the core of high streamwise velocities continues to shift toward the outer bank for some distance downstream of the region of high channel curvature. This momentum-induced lag means that the flow is still close to the outer bank close to, or at the point where curvature changes sign.

In alluvial channels, as sediment deposits along the inner bank, the flow starts moving away from the inner bank, towards the deeper regions within the channel. As a result, a pool is created near the outer bank. This is an example of topographic steering effects that are due to the redistribution of the streamwise velocity in the cross section due to the large scale features of the bathymetry. Thus, to be able to confidently use results of numerical simulations to understand the flow physics and to estimate the capacity of the flow to erode the bed and the banks in natural streams, the numerical model has to be capable of accurately predicting the large-scale coherent structures associated with the secondary flow and the turbulent flow structure.

To a first approximation, the strength of the secondary flow (e.g., as measured by the circulation of the main cell) varies monotonically with the ratio of the local curvature radius, R, to the channel width, B. As R/B decreases, the degree of nonlinearity of the interactions between the secondary cross-stream flow and the streamwise momentum increases. Moreover, these interactions increase the anisotropy of the cross-stream turbulence. A classic example of anisotropic effects in curved channels is the formation of a secondary SOV cell close to the outer bank that rotates in the opposite direction compared to the main cell of cross-stream circulation (Blanckaert and de Vriend, 2004, Blanckaert, 2011).

LES has been used successfully by several groups to predict and understand the flow in bends of mild (R/B < 8) and medium (3 < R/B < 8) curvature. For example, Moncho-Esteve et al. (2010) used LES to predict flow in a compound meandering channel of medium curvature with flat bed and to study the effects of the floodplain on the channel flow at flood conditions. In the present section we will discuss results of well-resolved LES (no wall functions) using the dynamic Smagorinsky model (section 2.4) and of DES using the Spalart-Allmaras model (section 3) to illustrate the capability of eddy resolving techniques to capture the mean flow and turbulence structure in high curvature bends.

Given the extensive set of measurements conducted by Blanckaert (2009, 2010) for a 193^0 bend with R/B = 1.3 (Fig. 1), we focus on the simulation of two test cases corresponding to flat bed and equilibrium bathymetry obtained for a continuous constant influx of sediment that moved as bed load (Fig. 4). More details on the DES simulation of the deformed bed case are given in Constantinescu et al. (2011a). The same test cases were investigated by van Balen et al. (2010a, 2010b) using LES with wall functions and the classical Smagorinsky sub-grid scale model. Results of RANS simulations are also included to better assess the predictive capabilities of LES and DES for flow in curved channels. In the following, we will evaluate the predictive capability of eddy resolving techniques for flow in a sharply curved bends based on their ability to resolve the distribution of the streamwise velocity and streamwise vorticity in relevant cross sections and to capture the formation of SOV cells near the outer and inner bank, as revealed by experiment (note that recent field studies have detected SOV cells in mildly and tightly curved meander bends, e.g. Sukhodolov (2012), Schnauder and Sukhodolov (2012)). Given a streamwise coordinate, ξ, and corresponding velocity component, u_ξ, transverse component, y (u_y) and vertical component z, (u_z), the streamwise vorticity, ω_ξ is defined as:

$$\omega_\xi \equiv \omega_{yz} = \frac{1}{2}\left(\frac{\partial u_y}{\partial z} - \frac{\partial u_z}{\partial y}\right) \qquad (15)$$

as defined under (12). In this study, we non-dimensionalise ω_ξ by *D/U* where *D* and *U* are the channel depth and bulk velocity in the upstream part of the inlet straight reach.

In the two test cases, *B/D* = 8.2 and Re = *U D* / *ν* ≈ 68 000, and *ν* is the kinematic viscosity of water. The channel sidewalls were vertical and smooth. The length of the outflow straight reach was around 30 *D*. The boundary conditions in the LES simulation of the flat bed case and in the DES simulation of the deformed bed case were similar. Turbulent inflow conditions corresponding to fully-developed turbulent channel flow with resolved turbulent fluctuations were applied. A steady fully-developed pre-calculated RANS solution was used to specify the inflow conditions in the RANS simulations (Zeng et al., 2008). At the outflow, a convective boundary condition was used in DES and LES. All the solid surfaces were treated as no-slip boundaries. The equivalent total bed roughness in the deformed bed case estimated using the procedure described by Zeng et al. (2008) was 0.037 m. The free surface was treated as a rigid lid. This simplified treatment is justified because the Froude number was smaller than 0.4. The computational domain in LES and DES was meshed using 9-12 million cells. The mesh size in the wall normal direction was close to two wall units at the channel bed and the two banks. The mesh was then stretched such that in the centre of the channel the grid size in the horizontal directions was about two times the grid size in the vertical direction close to the free surface. This is in accord with the recommendation we provide for mesh resolution in section 6 of this manuscript.

In the flat bed case, the main cell of cross stream circulation occupies most of the section (Fig. 3). Comparison with RANS simulations and experiment shows that LES is much more successful in predicting the distribution of the streamwise vorticity, ω_ξ, in the channel (Fig. 2). The region of high (positive) ω_ξ in sections D120 and D180 that runs continuously from the outer wall to the inner wall close to the channel bottom and then extends upwards parallel to the inner wall toward the free surface is induced by the main cell. RANS severely underpredicts the strong amplification of ω_ξ near the bed and the inner wall, and the size of this region compared to experiment. By contrast, LES predictions agree quite well with measurements. Moreover, RANS does not capture the secondary SOV cell forming close to the inner wall. In section D120, this SOV is visualized as a nearly circular patch of high (positive) ω_ξ situated close to the free surface and the attached boundary layer on the inner bank. The overall level of agreement between the present LES predictions of ω_ξ and the LES with wall functions reported by van Balen et al. (2010a) is about the same. A more quantitative way of estimating the strength of the secondary flow based on the streamwise vorticity distributions provided in Fig. 2 is to calculate the circulation associated with the main cell of cross stream circulation which is simply the integral of the streamwise vorticity over the main cell region (e.g., region of positive streamwise vorticity). LES predictions of the circulation were within 5% of value inferred from experiment which is very good agreement. The error in RANS was more than double at most sections.

As shown by the 2-D streamline patterns in Fig. 3, RANS does not capture the formation of the secondary SOV cell at the outer-bank. LES predicts such a cell is present from section D30 to section P1.0 situated inside the straight exit reach. The LES with wall functions of van Balen et al. (2010a) also captured the presence of the outer bank cell, but the cell extended only over the upstream part of the bend. The fact that well-resolved LES predicts an outer bank cell extending over the whole length of the curved reach is consistent with experimental measurements.

The curvature induced interaction between the streamwise velocity and the secondary flow in the deformed bed case is even more complex due to topographic steering effects induced by the riffle-pool bathymetry developing at equilibrium conditions (Fig 4). Experiment and DES results show that the flow separates in horizontal planes in the deformed bed case (Fig. 5). This is consistent with findings of several studies conducted in sharply curved river reaches that have shown the flow can separate close to the inner bank (e.g., Leeder and Bridges, 1975, Ferguson et al., 2003, Frothingham and Rhoads, 2003) and in the lee of submerged point bars (Frothingham and Rhoads, 2003). In the case analyzed here, two recirculation eddies form over the shallowest regions situated close to the inner bank. They are bordered by strong separated shear layers inside which highly energetic vortical eddies are shed. The distribution of the vertical vorticity in the instantaneous flow fields (e.g., see Fig. 5) shows that close to the free surface some of the eddies convected in the downstream part of the separated shear layer originating around section D30 can penetrate until the outer bank. In the case of a channel with loose banks, this can result in further outer bank erosion close to section D90 where also the strength (e.g., as measured by circulation) of the secondary flow is the largest.

Figure 4 also visualizes the SOV cells present in the deformed bed case and their position within the bend. The visualisation technique used is a commonly adopted in fluid mechanics and is known as the *Q*-criterion (Dubief and Delaycre, 2000). The SOV cell denoted V1 corresponds to the main cell of cross-stream motion. The large vortical structure present in the central part of the curved reach starting around section D60 is associated with the shear layer forming on the outside of the point bar and main recirculation region. The 2-D streamlines and vertical vorticity contours in Fig. 5 visualize the recirculation eddy and the separated shear layer, respectively. Finally, three other SOV cells are present close to the inner bank. Consistent with experiment, no secondary SOV cell is predicted at the outer bank in the deformed bed case.

Figure 6 compares the streamwise vorticity distributions predicted by experiment, DES and RANS in sections D60 and D120. The patch of high (positive) streamwise vorticity magnitude situated within the deeper (outer bank) side of these two sections D60 and D120 corresponds to the main cell of cross-stream circulation, V1 (see also Fig. 4). RANS predictions of the vorticity amplification within the core of V1 are in reasonable agreement with experiment and DES at section D60 where the total circulation associated with the core of V1 is within 30% of the experiment. Meanwhile, RANS fails to capture the region of high amplification of ω_ξ within the core of V1 observed in experiment and DES at section D120. The other important difference between the ω_ξ distributions predicted by DES and RANS in section D120 is observed close to the inner bank where an SOV cell (V3) is forming. Though V3 is situated outside the region where velocity measurements were performed, the increased scour near the inner wall suggests the presence of a strongly coherent (high circulation) SOV cell at that location. The circulation of V3 is more than two times larger in DES compared to RANS. DES results show that the cores of the SOV cells are regions in which the turbulent kinetic energy levels are several times larger than those in the incoming fully developed turbulent flow (e.g., see Fig. 7 for section D120). This suggests the cores of the SOVs are subject to large-scale oscillations in the instantaneous flow.

A more accurate prediction of the streamwise velocity and streamwise vorticity in the curved channel should result in more accurate predictions of the bed shear stress and of the depth-averaged horizontal velocity components that are used by the sediment transport module in codes that have the capability to predict the channel morphodynamics. Of course, one has to keep in mind that there is lots of empiricism associated with the way sediment transport, and in particular bed load transport and the flux of entrained sediment, are modelled and that these models were calibrated based on simpler experiments performed in the laboratory with generally fine sediment of one size. Additional calibration and corrections will probably be needed when these models are applied at field scale. However, by resolving the time-varying flow, eddy resolving methods have the potential to improve predictions for sediment transport, particularly under marginal transport, as is discussed in section 4.4.

While DES predicted the largest bed shear stresses to occur between sections D30 and D120 in the deformed bed case (Fig. 8), RANS predicted the largest bed shear stresses to occur much farther downstream, in between sections D70 and D180 (Constantinescu et al., 2011). The field study by Ferguson et al. (2003) of a channel with a natural pool-riffle topography and strong inner bend curvature (R/B < 1.4) found that the region of maximum boundary shear stress at the outer bank was situated mostly upstream of the bend apex, where a separated flow region similar to the one observed in the deformed bed case was present, rather than downstream of it. This is consistent with the distribution of the nondimensional bed shear stress predicted by DES in Fig. 8. The boundary stress, τ, in Fig. 8 is nondimensionalized by the average value of the boundary shear stress in the inlet section, τ_0, where the flow is fully developed. Additional information revealed by DES is that the transverse component of the bed shear stress becomes comparable to the streamwise component over the high transverse-bed-slope region near the outer bank, situated in between sections D30 and D120. This region roughly corresponds to the one where the coherence of V1 is the highest. Downstream of section D120, the compactness of the core of V1 decreases strongly (Fig. 6). Thus, the capacity of V1 to induce large transverse bed shear stresses decreases. This detailed information on the distribution of the bed shear stress helps understand the evolution of the bathymetry toward equilibrium.

Compared to the corresponding LES simulation employing wall functions, the DES simulation of the deformed bed case predicted some features of the secondary flow more accurately, when benchmarked against experiments (see discussion in Constantinescu et al., 2011a). The primary reason for the success of DES was not so much due to the different sub-grid scale model used in LES mode by DES (the Reynolds number was relatively low and, thus, the effect of the subgrid scale model on the mean flow was fairly limited), but rather to the fact that DES, similar to well-resolved LES, did not use wall functions. Thus, one can conclude that well-resolved LES and DES can accurately predict secondary flow and its effect on the velocity redistribution within sharply curved bends at all stages of the erosion and deposition process. Simpler eddy-resolving models (e.g., LES with wall functions) are also much more successful than RANS models, but do not capture some of the quantitative and qualitative features of the secondary flow in strongly curved channels due to the simpler treatment of the near-wall region. This has obvious consequences for simulation of flow, turbulence structure and sediment entrainment mechanisms in natural river reaches.

4.2 Confluences

At natural confluences, the convergence of flow induced by the configuration of the two incoming channels results in a highly three-dimensional flow and the production of large-scale turbulence. In particular, the flow and turbulence structure at river confluences between non-parallel streams are characterized by the formation of a mixing interface (MI) and, in many cases, of streamwise-oriented vortical (SOV) cells on the sides of the MI (Paola, 1997, Rhoads and Sukhodolov, 2001). Depending on the angles between the two incoming streams and the downstream channel, and the velocity and momentum ratio between the incoming streams, the MI can be in the Kelvin-Helmholtz (KH) mode or in the wake mode, following the classification introduced by Constantinescu et al. (2011b). When the KH mode dominates, the MI contains predominantly co-rotating large-scale quasi 2-D eddies whose growth is primarily driven by the KH instability and vortex pairing, similar to the classical case of a shallow mixing layer developing between two parallel streams of unequal velocities (Babarutsi and Chu, 1998). When the wake mode dominates, the MI is populated by quasi 2-D eddies with opposing senses of rotation that are shed from the junction corner region as a result of the interaction between the separated shear layers on the two sides of the junction corner. The eddy structure of the MI in the wake mode is similar to the von Karman vortex street that forms behind cylinders and other bluff bodies. At natural stream confluences both modes can simultaneously influence the development of eddies within the MI, but often one mode will dominate over the other. Flow conditions, confluence geometry, and bathymetry will determine which mode is dominant.

The SOV cells forming on one or both sides of the MI are regions of strong helical motion that significantly affect momentum and mass exchange processes at confluences for which the angle between the two incoming streams is large. In such cases, the two streams approaching the MI have significant transverse momentum with respect to the direction of the MI (Rhoads and Sukhodolov, 2008). The convergence of the flows results in an increase of the elevation of the water surface along the MI, which in turn induces strong downwelling of the fluid along the MI. The descending fluid moves laterally first away from the MI and then rises toward the free surface. The result is the formation of a pair of counter-rotating vortices (primary SOV cells) parallel to the orientation of the MI. Evidence for the formation of primary SOV cells is quite strong for confluences with a concordant bed (e.g., see Paola, 1997, Rhoads and Sukhodolov, 2001, Sukhodolov et al., 2010). Flow structure at natural stream confluences is further complicated by topographic steering effects induced by bar forms on the channel bed and by large-scale irregularities of the channel banks (Rhoads and Sukhodolov, 2001).

Both types of MIs were observed in field investigations of the flow and turbulence structure at the confluence of the Kaskaskia River and Copper Slough stream in Illinois, USA conducted by Sukhodolov and Rhoads (2001) and Rhoads and Sukhodolov (2001). The upstream channel for the Kaskaskia River (KR) is fairly well aligned with the downstream channel. The Copper Slough (CS) joins the Kaskaskia River at an angle of about 60^0. The cross sections of both tributaries upstream of the confluence are trapezoidal. The inner and the outer banks correspond to the east (E) and the west (W) banks, respectively (see Fig. 9).

The results discussed in this section are for two sets of flow conditions recorded at this river confluence that were investigated by Constantinescu et al. (2011b, 2012) using DES. The code and DES model were the same as the one used to perform the DES simulations of flow in open channel bends discussed in section 4.1. In the first test case (Case 1) the momentum ratio (Copper Slough to Kaskaskia), Mr $\cong$ 1 and the Reynolds number is Re = 166 000 based on mean values of velocity, U, and flow depth, D, in the main channel. In Case 2, Mr $\cong$ 5.5 and Re = 77 000. The mean flow depth of the main channel in Case 2 was about two thirds of that in Case 1. The change in the momentum ratios means that the wake mode is dominant in Case 1, while the KH mode is dominant in Case 2. For both test cases, every quantity was non-dimensionalized using the U and D values for Case 1, i.e., U = 0.45 m/s and D = 0.36 m.

For both test cases, inflow conditions corresponding to fully-developed turbulent channel flow with resolved turbulent fluctuations were applied. A convective boundary condition was used at the outflow of the domain. The free surface was modelled as a shear-free rigid lid. Transport of mass in the vicinity of the MI was investigated by solving an advection-diffusion equation for a passive (conserved) tracer. A tracer with a normalized concentration of 1 was introduced continuously at all flow depths in two small regions situated around the junction corner. The concentration of the tracer in the two incoming streams was equal to zero. The flux of tracer was set equal to zero at the channel bottom, free surface, and the banks. The computational domain was meshed with close to 5 million cells. The wall-normal grid spacing of the first row of cells off the bed and the banks was less than two wall units.

The position of the MI (Fig. 9) and the mechanisms responsible for the formation and the dynamics of the MI eddies are different in the two cases. In Case 1, the MI was situated within the central part of the downstream channel. In Case 2, the much larger value of the momentum of the Copper Slough stream and the presence of a very shallow region close to the east bank in between sections B and C was the reason why the MI moved toward the west bank. The position of the MI in both cases was in good agreement with that inferred from field data. The large-scale eddies advected inside the MI were found to be quasi two-dimensional (2-D) and to have their axes close to vertical in both cases.

Despite the fact that the position of the MI with respect to the two banks changed considerably, a system of strongly coherent SOV cells developed on the two sides of the MI in both cases (Fig. 10). In Case 1, the circulations of the SOV cells on the two sides of the MI had similar magnitudes (within 50% of each other downstream of section A2). The circulation was estimated by integrating the out-of-plane vorticity within the core of the vortex with respect to a plane that was close to perpendicular to the axis of the vortex at a given location. The Q-criterion (Dubief and Delcayre, 2000) was used to identify the core of the vortex or SOV cell. In Case 2, the much larger momentum of the Copper Slough stream induced SOV cells of larger coherence and circulation on the Copper Slough side of the MI. The SOV cells on the Kaskaskia River side were quite weak in Case 2, even in the upstream region of the MI where the Kaskaskia River approaches the MI at a high angle. For example, the ratio between the circulations of the SOV cells on the two sides of the MI was close to 3.5 between sections A3 and A.

In both cases, the SOV cells were found to play a very important role in the redistribution of the streamwise velocity on the two sides of the MI within the confluence hydrodynamics zone. For example, in Case 1, DES predicts two distinct regions of large streamwise velocity, u_s, within the upper part of section A (Fig. 11). DES results show that the circulation of the SOV cell on the east side (SVE1) is larger than that on the west side (SVW1). This is the main reason why the core of high u_s values in the central part of section A is displaced toward the east bank. All these features of the distribution of u_s, in section A are in good agreement with field measurements in the same section. It is relevant to mention that a RANS simulation run on the same mesh with similar boundary conditions did not predict the formation of two distinct regions of relatively high u_s values close to the free surface. The comparison between the distributions of u_s predicted by DES and RANS and the field experiment in section C (Fig. 11) clearly favour DES. In particular, DES predicts the largest streamwise velocities occur close to the bed, in the central part of section C, which agrees well with the experimental measurements. Meanwhile, RANS predicts a much more uniform distribution of the velocity in the central part of section C with the maximum u_s situated close to the free surface. The main reason for the higher accuracy of DES predictions of the streamwise velocity distributions is the severe under prediction by RANS of the coherence and circulation of the main SOV cells (Constantinescu et al., 2011b).

The availability from DES of the instantaneous 3-D flow fields within the vicinity of the MI allows a detailed investigation of the dynamics of the SOV cells. In both cases, DES results show that the core of the SOV cell on the side of the incoming stream making a large angle with the downstream channel is subject to large-scale bimodal oscillations toward (interface mode, IM) and away (bank mode, BM) from the MI. As opposed to the flow in the incoming two streams, and even to the flow within the MI where the histograms of the velocity components contain only one peak (e.g., see Fig. 12a), the histograms of the spanwise and vertical velocity components contain two distinct peaks within the region where the core of SVE1 is subject to large-scale bimodal oscillations (e.g., see Fig. 12b). The main consequence of the presence of bimodal oscillations is a large amplification of the turbulence. For example, the distribution of the non-dimensional mean pressure fluctuations $\overline{p'^2}/\rho^2U^4$ in section A1 (Fig. 13) shows two spots of high mean pressure fluctuations within the region where the core of SVE1 switches aperiodically between the interface mode and the bank mode. The maximum values of $\overline{p'^2}/\rho^2U^4$ in this region are close to ten times larger than the ones observed in the surrounding turbulent flow. The presence of bimodal oscillations also explains why transverse velocity fluctuations in the field experiment with $\mathrm{Mr} \cong 1$ were comparable to or larger than streamwise velocity fluctuations in the central part of the cross-sections downstream of the junction corner. In both cases, the largest bed friction velocities were recorded beneath the region where the core of the primary SOV cell was subject to strong bimodal oscillations (Constantinescu et al., 2012). In Case 2, the bimodal oscillations were weaker than those observed in Case 1 and limited to the region where the central part of the incoming higher-momentum stream collided with the MI (Constantinescu et al., 2012). As the capacity of the SOV to entrain sediment is greatest in the regions where bimodal oscillations are present (Constantinescu et al., 2012), the differences in cell development and dynamics between the two cases will affect where sediment will be predominantly entrained around the MI region and how the confluence scour hole will develop in time.

In Case 1 (Fig. 9a), the eddies shed from the junction corner region have opposing senses of rotation. Their growth in size is not accompanied by a noticeable increase in their circulation. Thus, their capacity to entrain sediment from the bed at large distances from the junction corner is limited. The dynamics of the MI eddies downstream of section C is strongly affected by their interaction with energetic eddies forming in the region where the incoming flow in the Kaskaskia River is advected over a submerged block of failed bank material along the west bank near section A3. This induces a shear layer containing energetic eddies that is visualized using a green dashed line in Fig. 9a. Additionally, a highly energetic shear layer develops due to an abrupt lateral decrease in streamwise velocity toward the east bank downstream of section A1. This is induced by the sharp curvature of this bank. This shear layer is visualized using a black dash-dot line in Fig. 9a. The development of inner bank shear layers are a general characteristic of flow in sharply curved open channels with flat or deformed beds (Constantinescu et al., 2011a). By contrast, the water level in Case 2 was sufficiently low that the flow does not submerge the block of failed material around section A3 (Fig. 9b). This is why large-scale energetic eddies are absent on the Kaskaskia River side in Case 2. Overall, this shows that depending on the flow conditions, the large-scale bathymetry and bank features can significantly affect flow and turbulence structure in the confluence hydrodynamics zone and the dynamics of the MI eddies at natural confluences.

The mixing interface developing at most large river confluences can be considered as shallow. A fundamental issue related to shallow mixing interfaces in which the KH mode is dominant is to estimate the distance from the origin of the MI at which the quasi-2D eddies stop growing and start losing their coherence and, hence, their capacity to entrain and transport sediment outside of the confluence hydrodynamics zone. Eddy resolving techniques can be used to estimate this distance. Figure 15 shows the structure of the MI at a symmetric confluence between two streams making an angle of 60^0 for which the velocity and momentum ratios are equal to two and the channel Reynolds number is equal to 200 000. The channel depth in the two incoming streams and the main channel is constant and equal to *D*. Similar to Fig. 14, the MI eddies are visualized close to the free surface using a passive scalar introduced continuously near the confluence junction corner. The width of the downstream channel is about 70*D*, which is sufficient to avoid interactions of the eddies advected within the MI with the regions of separated flows situated close to the banks. The channel length downstream of the confluence apex is more than 500*D*, which is enough for the growth of the MI eddies to cease and the coherence of these eddies to decay. DES shows that the average diameter of the MI eddies attains close to 17*D* at around 170*D* from the confluence apex (around section H in Fig. 15). Results in Fig. 15 show that similarly to the case of a shallow mixing layer developing between two parallel streams (Chu and Babarutsi, 1988), the shape of the MI becomes undulatory and the coherence of the quasi-2D eddies is gradually lost at large distances from the origin (e.g., past section H in Fig. 15). Experiments that try to study the flow structure and to estimate sediment entrainment capacity at such shallow confluences are very difficult to set up in the laboratory because of limitations in the length and width of the flumes in which the experiments are generally conducted.

4.3 Rough beds

In gravel bed rivers, the micro-topography of the bed exerts a significant effect on the generation of turbulent flow structures. This micro-topography scales from individual gravel particles through pebble clusters to large-scale bed forms (Brayshaw *et al.,* 1983; Robert *et al.,* 1993). Furthermore, flow in gravel bed rivers is typically shallow, and the relative submergence of particles (ratio of mean flow depth to typical roughness height) seldom exceeds 10–20 in floods and can be less than 5 during base flow conditions. In such shallow flows, the microtopography of the bed exerts a significant influence on the generation of turbulent structures (Wiberg and Smith, 1991; Dinehart, 1992) and localized topographic forcing of flow may provide a dominant mechanism for momentum exchange. Such structures are related to the wakes of individual obstacle clasts, and jetting of higher-velocity flow between such clasts, which is commonly thought to be in the form of a horseshoe vortex formed upstream of clasts, and shedding of vortices in the lee of the cluster (Robert *et al.,* 1992, 1993; Kirkbride, 1993), with the upstream horseshoe vortex being analogous to a simple juncture vortex (Brayshaw *et al.,* 1983; Best, 1996). Here, a region of weak recirculation is caused by flow stagnation and separation immediately upstream of the object, which leads to the generation of vorticity that can, in turn, trigger the formation of large-scale turbulent flow structures. These are large-scale eddies that scale closely with the flow depth (h) in the vertical and approximately 2h in the lateral spanwise direction. The downstream scale of these structures appears to be dependent upon both bed roughness (Sukhodolov et al., 2011) and hydraulic conditions: the greater the flow depth and velocity, the more pronounced the development of the coherent flow structure (Shvidchenko and Pender, 2001). The downstream scale of these structures has been proposed to be between 4*h* and 7*h*, with this scale increasing as bed roughness decreases (Klaven, 1966; Klaven and Kopaliani, 1973; Shvidchenko and Pender, 2001).

To date our understanding of these processes have either come from physical scale experiments, e.g. Shvidchenko and Pender (2001), Hardy *et al*. (2009, 2010) or field based studies that are limited because of the challenges of instrumenting such phenomena (Roy *et al.,* 1996). However, the application of LES or DES has the potential to further our process understanding of such flows although, as yet, there have been a limited number of applications. Most computational fluid dynamics (CFD) applications to natural gravel bed rivers have been applied at a larger spatial scale and boundary fitted coordinates, which involve mesh deformation in the Cartesian space (though not in the computational space), have been used to represent the channel geometry. The bed micro-topography is represented parametrically through an exaggerated value of the roughness height in a log law representation of flow in the cells adjacent to the bed. This has two main disadvantages. Primarily, boundary fitted coordinates generate mesh deformation that may increase numerical diffusion, which will increase as the resolution of spatial discretization increases (as the topographic information becomes more complex). Secondly, the micro-topography representation involves specification of a friction height (z_o) in some sort of wall function and the multiplication upward of the equivalent sand grain roughness.

These difficulties can be avoided using high resolution solutions to the flow equations (see sections 4.1 and 4.2). However, such approaches are highly computationally intensive and an alternative approach that attempts to move beyond the wall function approach to represent irregular micro-topography accurately, is to include the bed geometry explicitly through a Mass Flux Scaling Algorithm (MFSA) (Lane *et al.,* 2002, 2004;

Hardy *et al.,* 2005, 2007) where the cell volume and faces are scaled and blocked according to the amount of topography included in the mesh. This uses a porosity method based upon the work of Olsen and Stokseth (1995) and involves the use of a regular structured grid in which all control volumes are orthogonal in both computational and Cartesian space, with the bed topography specified using cell porosities.

Here we report the results of a shallow flow over a natural gravel bed river using LES. The study used a standard Smagorinsky model within the MFSA to assess if the approach produces physically realistic results. The experimental setup used was the same as used by Hardy *et al.* [2007]. It is based upon water worked gravels (D_{50} = 0.020 m; D_{84} = 0.069 m) in a 0.30 m wide and 8.0 m long tilting flume. The surface morphology was measured using two media digital photogrammetry (see Butler *et al.* (2002) for a full explanation) providing the necessary topographic information (Fig. 16) at a spatial resolution of 0.001 m with a mean surface error of 0.0008 m and root-mean square error of ±0.0017 m. Shallow, low flow conditions were considered with a depth-averaged inlet velocity of 0.24 ms^{-1}, a flow Reynolds number of approximately 11 000 and a Froude number of 0.31 equating to a $d/D_{50} \approx 3$ and $d/D_{84} \approx 1$. A RANS simulation of flow over this topography was used to hot-start the simulations and cyclic boundary conditions were applied at the inlet, while at the sidewall, no-slip conditions were used. The simulation was run for 102.4 seconds at 10Hz.

Figure 16 shows a series of velocity magnitude (the resolved components of *u*-, *v*- and *w*-) plots of a series of slices across the gravel surface. Each image is spaced 1 second apart. The images show a strongly streaky pattern, with areas of fast shearing flow around large particles (A in Fig. Xa) and wakes in the lee of such particles (e.g. B in Fig. 16a). In region A (Fig. 16a) a region of high flow velocity arising from flow separation around a large protruding particle can be observed. This appears to be quasi stationary, its core being present in all of the images covering the 6 second period, although pulses of higher velocity can be seen to evolve and the move downstream (e.g. Fig. 16b & c). These features appear similar to the large flow structures previously observed by Shvidchenko and Pender (2001) and have similar characteristics to the horseshoe vortex observed in classic fluid mechanics. In region B there is a relatively stable region comprising a low momentum recirculation cell (i.e. a wake) with possibly an arch vortex similar to that identified by Hunt *et al*. (1978). Typically these features would have been predicted qualitatively by the application of a RANS turbulence closure model (e.g., Lane *et al.*, 2004), although time averaged turbulence models (e.g. the two equation k-ε model) are poor at predicting the exact form of separation and reattachment processes (Lien and Leschziner, 1994; Hardy *et al*., 2005). However, when a plan view of the flow magnitudes is shown (Fig. 17) regions of flapping, downstream from the object are observed. At z/h = 0.5 (Fig. 17 a-c) streaks of high magnitude velocity are seen to flap and interact (Region C) demonstrating 'packets' of flow moving downstream. Higher in the flow (z/h = 0.8, Region D) demonstrate the growth and shortening of high magnitude flow in the bed. This heterogeneity of the near-wall flow environment, which would not be correctly simulated using a time-averaged simulation, indicates that to understand pollutant dispersal, sediment erosion and deposition processes, and salmon spawning habitat in gravel-bed rivers, requires the explicit treatment of large-scale, time varying eddy structure.

4.4 Sediment entrainment and transport from the perspective of eddy resolving simulations

The non-dimensional shear stress, θ, developed by Shields provides the underpinning of a great many studies on bedload entrainment (Wilcock, 1993; Buffington and Montgomery, 1997). However, given the data available from the field, there are different ways to estimate the dimensional shear stress, τ, in the relation $\theta = \tau / [(\rho_s - \rho)\, g\, D]$, where D is the grain size of interest, ρ_s and ρ are the densities of sediment and fluid, respectively and g is gravitational acceleration. If one only knows the channel slope and flow depth, the depth-slope product may be used, while if a mean velocity profile is available (from field data or a RANS numerical simulation), one can use the product of the fluid density and the square of the shear velocity. If the Shields parameter is calculated on the basis of these expressions it is well-known that sediment entrainment can take place below a notional critical threshold for sediment movement and this is termed marginal transport (Andrews, 1994). Clearly, in such situations, movement is occurring both because of the unusual status of some particles with respect to packing density, exposure and projection, but also because of the occasional action of turbulent stresses such that the critical Shields parameter is exceeded locally for a small period of time. This is particularly likely to occur due to flow separation and shear layer generation around individual clasts on the channel bed (Buffin-Bélanger and Roy, 1998) in coarse bedded channels.

The RANS equations contain a source term that incorporates the average effect of turbulence on the mean flow – the Reynolds stresses (eq. 8). Hence, if one has a resolved RANS simulation, the Reynolds stresses should prove to be useful in characterising sediment entrainment under conditions of marginal transport, permitting one to go beyond simple mean flow based approaches to sediment movement. However, it has been clearly documented for some time now that Reynolds stresses are not a good measure of the effectiveness of turbulent flows for mobilising sediment (Heathershaw and Thorne, 1985; Nelson et al., 1995). This is clear from a consideration of the different ways that terms may make a positive or negative contribution to the Reynolds stresses. A positive stress will be exerted on the mean flow when either more rapidly moving flow moves towards the bed (quadrant 4), or when slower moving fluid moves away (quadrant 2). Similarly, negative stresses result from slower moving fluid moving towards the bed (quadrant 3) or faster fluid moving away (quadrant 1). The Reynolds stress is an average across these processes yet bedload entrainment is clearly coupled to quadrants 1 and 4, (Heathershaw and Thorne, 1985) while entrainment into suspension correlates with quadrant 2 (Niño and García, 1996). Thus, a high Reynolds stress resulting from a great deal of quadrant 2 events could mean a high propensity for suspension entrainment, but little bedload, while one dominated by quadrant 4 would mean the opposite, with no means available to discriminate between these cases. Similarly, if the Reynolds stress is low, this could be because of little turbulence, meaning little potential for entrainment, or because large quadrant 1 and 4 events cancel each other, meaning a high potential for bedload motion.

The deficiencies of the Reynolds stress approach indicate the potential for eddy-resolving methods in sediment motion as force-moment balances on a grain can be resolved based on instantaneous velocities (Komar and Li, 1986; Wiberg and Smith, 1985) or, following recent developments, if one adopts an impulse based approach (Diplas et al., 2008; Valyrakis et al., 2010), the instantaneous velocities can be integrated over the known duration of a flow event as all such information is now available. Experiments of the type undertaken by Schmeeckle et al. (2004) have highlighted the complexity of flow around individual grains at a scale below that discussed in the previous section. If such processes are important under marginal transport conditions then eddy resolving methods offer an attractive means for obtaining relevant information. Work by Chang et al. (2011) has shown using DES that predicted scour holes in the wake of obstacles are liable to be much greater than is predicted from using RANS owing to the enhanced ability to replicate instantaneous forces effectively.

Given that a particle is entrained into the flow as suspended material or is mobilised as a rolling or saltating bedload particle, its trajectory will be modified as it is acted upon by different parts of the flow at different times. Clearly eddy-resolving methods again have the advantage that such information is available. Hence, a Lagrangian model for sediment movement may be coupled to an LES/DES in a more physically realistic way than is possible with other techniques. An example of this latter approach is provided by the recent work of Escauriaza and Sotiropoulos (2011) who studied flow in the wake of a cylinder where eddy-shedding plays an important role in sediment movement. The DES captured the relevant physics of this vortex system appropriately and was coupled to a Lagrangian model for sediment motion using one-way coupling (i.e. the particle motion does not feed back onto the flow field, which is a standard assumption made in geomorphological models). This approach was able to simulate a variety of features observed in laboratory experiments including intermittent transport, motion by both sliding and saltation, and the formation of streaks by near-wall vortices. Thus, although such studies are currently rare and require significant computational effort, they demonstrate that eddy-resolving simulations contain sufficient physics to model the detail of bedload entrainment and motion under conditions of marginal transport effectively.

5. Issues regarding the validation of eddy-resolving numerical methods

The validation of numerical models is an important issue. It is particularly complex in the case of field-related problems in geomorphology, where field datasets have dramatic limitations, particularly in terms of spatial resolution. In addition, as models begin to incorporate more and more realistic flow physics, while model verification and grid independence studies are still needed (Hardy et al., 2003), validation is likely to become more focussed on the details of flow physics (flow structure characterisation) rather than on mean quantities. With one-dimensional and two-dimensional hydraulic models, dramatic simplifications to the underlying physics are made, which means that it is essential that one tests how successful such approximations are in modelling the flow. As one moves to a computational fluid dynamics framework, and then through RANS, DES/LES and toward direct numerical simulation of the Navier-Stokes equations, fewer approximations are made, meaning that there is greater confidence that the physics are appropriate. Moreover, DES/LES simulations conducted with codes that are at least second order accurate in both space and time and with subgrid scale models that correctly predict a zero eddy viscosity in regions where the flow is not turbulent (e.g., the dynamic Smagorinsky model) and on sufficiently fine meshes especially in the wall normal direction (see section 6) are likely to require less direct validation. Though a grid dependency study is not required for each new application of the LES/DES code, it is highly recommended such an exercise is undertaken at least one or two relevant test cases for which the relative level of mesh refinement expressed in non-dimensional wall units is comparable to the one used in the application of the model.

It is also important to decide what the relevant validation criteria are. Choosing the vertical mean velocity profile would be meaningless for a depth-averaged two-dimensional model that only yields one velocity averaged over the whole depth, but it would be appropriate for three-dimensional RANS and DES/LES as capturing the secondary flow and the redistribution of the streamwise momentum in the flow domain accurately is essential for geosciences applications in alluvial channels where these two variables determine to a large extent sediment transport and morphology changes. However, if one has chosen to adopt an eddy-resolving simulation, this may be because it is expected to improve estimation of mean flow parameters, but it is more likely that one wishes to extract something concerning the instantaneous flow structure and dynamics of the large-scale coherent structures that play an important role in bed/bank erosion and sediment transport. If for example, this is the distribution of instantaneous turbulent stresses over different flow quadrants, then a comparison to single-point estimates from field data may still be possible (with an appropriate consideration of the scale over which flow variables are averaged in time and space). If however, it is vorticity, swirling strength or similar, then validation is limited by the inability to derive such quantities from field data as they require simultaneous measurement of the flow at multiple neighbouring positions – something that is rarely possible, particularly in large channels. If the flow contains regions in which well-defined large scale vortices are advected (e.g., the mixing interface at a river confluence), then the peak frequencies obtained from field data velocity measurements can be used for additional validation and assessment of the predictive abilities of the unsteady RANS and especially DES/LES predictions. Velocity spectra measured in the field can be used for additional validation. Of particular importance, is whether the DES/LES simulation captures the presence of inertial -5/3 and/or of a -3 subranges. The former indicates the appropriate development of the scaling regime for three-dimensional flows where energy moves away from the forced scales towards the dissipative, while the latter is indicative of quasi two-dimensional structures (e.g., wake of islands, mixing interfaces developing in shallow channels). If these features are present in appropriate places then there is some confidence that the physics at scales smaller than the largest eddies is being modelled correctly.

A further consideration is the manner in which boundary conditions are input into the numerical model. As Fig. 16-17 show, bed roughness induces complex flow patterns.

Hence, accurate modelling of flow near the bed will require high resolution bathymetry. If this is not available and a RANS or eddy resolving model gives poor results near the bed, is this a failure of the model, or the way in which boundary conditions have been introduced into the model? Furthermore, in the field, with sediment transport potentially taking place in the near-bed region, it may be difficult to locate the height of the probe above the bed, and signals may decohere as suspended or bedload particles move through the measurement volume. Hence, is poor agreement a necessary flaw in the model or is it reflecting the complexity of undertaking precise field measurement?

Boundary conditions also include the specification of time series for each velocity component for each cell at the inlet to the domain. We discussed this issue briefly at the end of section 2, and Figure 18 indicates that there can be some sensitivity to the precise nature of the inlet conditions, but that in areas of complex missing, such effects are reduced. In this example, a precursor inlet simulation has been degraded in a controlled fashion using gradual wavelet reconstruction (Keylock, 2010). When the control parameter for this technique, ρ_{thresh}, is 1.0 the inlet conditions are identical to those from the precursor simulation, when $\rho_{thresh} = 0$, the values for each velocity component time series are identical to those in the precursor simulation and the Fourier spectrum is identical to some error tolerance, but the correlation between time series and the nonlinearity in an individual time series is destroyed. The other cases used represent intermediate conditions as described by Keylock et al. (2011). It is clear from this figure that failing to correctly preserve any of the correlation between time series degraded the pressure field on the face and top surface of the wall-mounted rib significantly. However, in the lee of the rib, there is very little difference between the simulations as the intense mixing decouples the flow before and after the rib. Hence, validation of a flow field exhibits some sensitivity to the nature of the inlet conditions, meaning that inlets need to be considered carefully in implementation (see section 6).

Here we propose two general strategies for validation, although with applications of eddy-resolving methods in geomorphology only emerging recently, a wider community consensus would be needed before firm guidelines can be provided. We would suggest that a two-pronged approach is useful:

(a) Validation using mean flow variables with a comparison to field data and, if applicable, dominant frequencies of the flow in regions where large scale eddies are present;
(b) Validation against laboratory experiments based on time-averaged and time-varying parameters.

Note that in both cases, we don't restrict validation criteria to flow parameters. For example, as shown by Kirkil and Constantinescu (2010) and Chang et al. (2011), use of eddy-resolving simulations can drastically change estimates of the size of an average scour zone as the resolved eddies contribute peak stresses and, thus, sediment entrainment events, that remain unresolved in RANS. Hence, a comparison of mean or equilibrium scour hole size between the field or experiment, and RANS and eddy-resolving simulations is useful. Successful validation is also predicated on comparable spatial resolution – comparing a mean estimated over a computational cell that is 0.01 m^3 in volume to data from an ADV averaged over 1 cm^3 is problematic. In this situation, if 0.01 m^3 is the greatest resolution attainable for reasonable computational cost, then extra thought needs to be given to the density of the data collected in the field to be used in validation. In general, the majority of validation variables will be derived from flow statistics. Clearly, if accurate data may be derived from multiple probes, to permit quantities such as vorticity or swirling strength to be measured directly in the field, that would be advantageous for validation. However, this is liable to be prohibitive in many situations. Hence, the recommendation that validation of a code's capability to replicate such phenomena is focused on laboratory work, where obtaining time-varying multi-point statistics to high precision is simpler.

Validation should also be conceived as a multiple-step process, progressing from simple cases to the field case. That is, initial validation of the same code for simpler cases for which detailed validation data exists from laboratory experiments conducted in controlled environments (e.g., under constant discharge, with well defined boundary conditions, etc.). For example in the case of a natural river confluence one expects the formation of a shallow mixing interface between the two incoming streams. It many cases, the channel curvature can be high close to the confluence region. Thus for this scenario, it is recommended the code is first validated by considering first the test case of channel flow in a curved bend and then the test case of a shallow mixing layer for which experimental data obtained at lower Reynolds numbers and in simplified channel geometries are available. Such data may include detailed vorticity and Reynolds stress measurements besides mean velocity and power spectra as well as visualizations of the instantaneous flow fields using PIV based techniques.

These suggestions do not resolve the question of what constitutes a validated simulation because, again, this is likely to depend on the quality, quantity and nature of variables available for validation. However, for mean flow variables, relative validation against RANS simulations is possible. If eddy-resolving methods are out-perfoming RANS methods in their representation of the mean flow field, when judged against field data, one will have some confidence that they are, at the very least, resolving the largest eddies to some accuracy, explaining the improved representation of the mean flow field. Hence, an output time series from a cell, low-pass filtered at a corresponding wavelength, is likely to be an adequate representation of the low-pass filtered equivalent processes in nature.

These validation issues are important as more and more DES/LES simulations are performed with commercial codes (e.g., Fluent, Flow3D) that now offer a wide choice of sub-grid scale models, time and space discretizations and mesh topologies. In many cases the users of such commercial codes have limited background knowledge in LES modelling and numerics. Thus, it is very important to consider something analogous to the validation steps articulated here before simulating a complex case with one of these codes and confidently using the data to understand the flow physics.

6. Some suggestions regarding the implementation of eddy-resolving methods in a geomorphic context.

Some pointers can also be given as to the design of eddy-resolving numerical experiments. However, as the state of the art for specific aspects of the numerical method, such as the modelling of the subfilter-scale or DES closures, changes through time, and because this paper pre-empts the wider use of these techniques, from which a consensus concerning implementation can be drawn, we fall short of trying to establish guidelines here. There are two main areas where considerations for eddy resolving methods potentially differ to RANS: the design of the numerical mesh, and the formulation of inlet conditions, and we focus on these here.

6.1 Numerical mesh aspects

An eddy-resolving simulation is likely to be started from a converged RANS. Grid independence assessments for the RANS (Hardy et al., 2003) provide a useful guide as to the minimum mesh required. However, DES and LES require a finer mesh than RANS, especially in the regions where dynamically important energy containing coherent structures are expected to form (e.g., separated shear layers, mixing interfaces, regions where large adverse pressure gradients are present). If one can estimate the size of the smaller eddies that need to be resolved, then an effective recommendation is that the mesh spacing is sufficiently fine to resolve those eddies using at least 6 points in each direction.

Constructing the mesh close to boundaries requires further consideration. Simulations must have a sufficiently fine mesh to resolve the flow near the channel bed and banks (the first grid point situated at less than 4 wall units from the bed and banks if the viscous sublayer is resolved, and at about 30-300 wall units if wall functions are employed). Then the mesh can be stretched such that close to the free surface the size of the grid in the vertical direction can attain close to 1/20 of the channel depth. The size of the mesh in the horizontal directions can be a couple of times larger, but ideally the shape of the cells should be as close as possible to a cube away from solid surfaces to resolve the 3D eddies with equal resolution in the three directions. This requirement is relaxed in shallow flows dominated by large quasi two-dimensional eddies.

As the size of the average cell increases relative to the turbulence scales in the flow, the demands placed on subfilter scale models are more intense. Clearly there are good fluid mechanics reasons why, for example, test filtering (Germano, 1992) is preferable to adopting a single value for the Smagorinsky coefficient. However, when the filter size is small, such that the resolved scales are some way into the inertial regime, the largest scales will be resolved well irrespective of the subfilter scale model. This is not the case when the filter scale is larger meaning that, in general, the resolution of the filter and/or mesh should increase as discussed above. However, there may also be benefits to moving to a more sophisticated subfilter scale closure for the simulation.

6.2 Inlet boundary conditions and simulation duration

As discussed in section 5 with respect to Fig. 18, adding a simple, spatially decorrelated noise to a mean signal, even if it has precisely the correct spectrum, will degrade the simulation relative to a time-resolved precursor simulation. However, this is a better strategy than just inputting a constant in time mean velocity field as at least it provides some pseudo-turbulence. (If merely the mean field is input, the inlet domain will have to be extended significantly for a reasonable turbulent flow to develop, or a bad simulation will result). Hence, our recommendation that in order to obtain a realistic flow at the inlet to the numerical domain, either a precursor simulation is used that can, in effect, be attached to the inlet, or the domain needs to be artificially extended such that a well-developed flow is created by the time the flow reaches the “true” inlet. In general, the former is much more computationally feasible. However, if upstream topographic steering is expected to have an effect on the inlet, then the latter may be useful as additional topographic data can be used to extend the length of the inlet region appropriately. Clearly, it is advantageous to define the inlet to a domain in a region where a developed flow is expected, reducing the need to measure inlet flow velocities to a high spatial and temporal resolution. If this is not possible then it would be adviseable to either spend significant time in the field characterising the inlet flow, or to undertake multiple simulations where the velocities applied at the inlet span the uncertainty in the field data.

The simulation needs to be run for sufficient time that initial numerical transients disappear and that bulk flow statistics have converged (including higher order moments than the mean, as we will often be interested in, at least, second order statistics such as variances and autocorrelations). However, if we are interested in coherent flow structures we then need a sufficient duration that individual eddies can be characterised statistically. Hence, we perhaps need a simulation with a duration that is twenty times or more the duration of the largest structures of concern. Storing all flow quantities from all cells for this period of time will not be feasible meaning that thought must also be given before the experiment as to the type of data and from where that is needed either for validation or for scientific interest.

7. Conclusion

In the last decade there has been significant growth in the use of eddy-resolving numerical methods in fluvial geomorphology and this paper has reviewed much of this work. Clearly, for a variety of flow processes of concern to the fluvial geomorphologist (flow in meander bends, through confluences and near rough boundaries), eddy resolving methods not only permit the dynamics of the large eddies and their role in mixing and sediment transport to be determined, but through the representation of such processes, also improve the manner in which the mean flow is resolved (e.g. Figures 3 and 11). Hence, we would argue that an understanding of the complex flows studied by geomorphologists would benefit from more widespread adoption of eddy-resolving methods.

Eddy resolving methods are computationally more intensive than Reynolds averaged methods and a well-resolved large-eddy simulation of a meander bend or confluence at sufficient resolution to negate the need for wall functions is likely to remain prohibitive to those without access to high performance computing. However, the emergence of hybrid RANS-LES methods such as detached eddy simulation (DES) in the last decade, as described in this paper, provides an effective compromise simulation technique that also has the advantage that an explicit wall treatment is not necessary if the near-wall mesh spacing in the wall normal direction is sufficiently fine. Discussion surrounding Fig. 3 in section 4.1 indicated that a fully-resolved LES out-performs one with wall functions as might be expected. However, Constantinescu et al. (2011a) also show that for geomorphic flows with significant secondary circulation, DES performs better than LES with wall functions, suggesting that DES provides a means for geomorphologists to undertake eddy-resolving simulations in field conditions in the future at reasonable computational cost. Given that these methods are implemented in various, widely available commercial codes, there are no significant proprietory issues concerning the adoption of these methods.

In conclusion, we hope that this review of eddy resolving techniques and the discussion of attempts to use these techniques in geomorphology, results in a growing adoption of these numerical methods. Hence, it might be possible in the medium term to establish relevant and community specific guidelines for the implementation of such techniques and the validation of model results. Sections 5 and 6 of this paper are our attempts to initiate such a process.

Acknowledgements

We are very grateful to the three referees and the editor who reviewed our manuscript for their suggestions and to the American Geophysical Union and Taylor and Francis for their permission to use some of the figures in this paper.

References

Aider, J.L., Danet, A., Lesieur, M., 2007. Large-eddy simulation applied to study the influence of upstream conditions on the time-dependant and averaged characteristics of a backward-facing step flow. J. Turbulence 8, 1–30.

Andrews, E.D., 1994. Marginal bed-load transport in a gravel-bed stream, Sagehen Creek, California. Water Resour. Res. 30, 2241-2250.

Aupoix, B., Spalart, P.R., 2003. Extensions of the Spalart-Allmaras turbulence model to account for wall roughness. Int. J. Heat and Fluid Flow 24, 454-462.

Babarutsi, S., Chu, V.H., 1998. Modelling transverse mixing layer in shallow open-channel flows. J. Hydraul. Eng. 124, 718-727.

Baldwin, B.S., Barth, T.J., 1991. A one-equation turbulence transport model for high Reynolds number wall-bounded flows. AIAA J. 91-0610.

Bates, P.D., Lane, S.N., Ferguson, R.I., 2005. Computational Fluid Dynamics: Applications in Environmental Hydraulics, Wiley-Blackwell, 540 pp.

Best, J.L., Roy, A.G., 1991. Mixing layer distortion at the confluence of channels of different depth. Nature 350, 411-413.

Biron, P.M., De Serres, B., Roy, A.G., Best, J.L., 1993. Shear layer turbulence at an unequal depth channel confluence. In Clifford N.J., French J.R., Hardisty J. (eds). Turbulence: Perspectives on flow and sediment transport. John Wiley and Sons. Chichester.UK. 360pp.

Blanckaert, K., 2009. Saturation of curvature-induced secondary flow, energy losses, and turbulence in sharp open-channel bends: Laboratory experiments, analysis, and modelling. J. Geophys. Res. 114, F03015, doi:10.1029/2008JF001137.

Blanckaert, K., 2010. Topographic steering, flow recirculation, velocity redistribution, and bed topography in sharp meander bends. Water Resour. Res. 46, W09506, doi: 10.1029/2009WR008303.

Blanckaert, K., 2011. Hydrodynamic processes in sharp meander bends and their morphological implications. J. Geophys. Res. 116, F01003, doi:10.1029/2010JF001806.

Blanckaert, K., de Vriend, H.J., 2004. Secondary flow in sharp open-channel bends. J. Fluid Mech. 498, 353-380.

Boano, F., Revelli, R., Ridolfi, L., 2011. Water and solute exchange through flat streambeds induced by large turbulent eddies. J. Hydrol. 402, 290-296.

Boussinesq, J., 1877. Theórie de l'écoulement tourbillant. Mémoires Présentés par divers Savants Acadamie Scientifique Institut Française 23, 46–50.

Brayshaw, A.C., Frostick, L.E., Reid, I., 1983. The hydrodynamics of particle clusters and sediment entrainment in coarse alluvial channels. Sedimentology 30, 137-143.

Brunke, M., Gonser, T., 1997. The ecological significance of exchange processes between rivers and groundwater. Freshwater Biol. 37, 1-33.

Buffin-Bélanger, T., Roy, A.G., 1998. Effects of a pebble cluster on the turbulent structure of a depth-limited flow in a gravel-bed river. Geomorphology 25, 249-267.

Buffington, J.M., Montgomery, D.R. 1997. A systematic analysis of eight decades of incipient motion studies, with special reference to gravel-bedded rivers. Water Resour. Res. 33, 1993-2029.

Butler, J.B., Lane, S.N., Chandler, J.H., Porfiri, E., 2002. Through-water close range digital photogrammetry in flume and field environments. Photogramm. Rec. 17, 419-439.

Chang, K., Constantinescu, G. and Park, S.O., 2007. Assessment of predictive capabilities of Detached Eddy Simulation to simulate flow and mass transport past open cavities. ASME J. Fluids Eng. 129, 1372-1383. DOI:10.1115/1.2786529

Chang, W.Y., Constantinescu, G., Tsai, W.F., Lien, H.C., 2011. Coherent structure dynamics and sediment erosion mechanisms around an in-stream rectangular cylinder at low and moderate angles of attack. Water Resour. Res. 47, W12532, doi:10.1029/2011WR010586.

Clayton, J.A., Pitlick, J., 2007. Spatial and temporal variations in bed load transport intensity in a gravel bed river bend. Water Resour. Res. 43, W02426, doi:10.1029/2006WR005253.

Constantinescu, G., Koken, M., Zeng, J., 2011a. The structure of turbulent flow in an open channel bend of strong curvature with deformed bed: Insight provided by detached eddy simulation. Water Resour. Res. 47, W05515, doi:10.1029/2010WR010114.

Constantinescu, G., Miyawaki, S., Rhoads, B., Sukhodolov, A., Kirkil, G., 2011b. Structure of turbulent flow at a river confluence with momentum and velocity ratios close to 1: Insight provided by an eddy-resolving numerical simulation. Water Resour. Res. 47, W05507, doi: 10.1029/2010WR010018.

Constantinescu, G., Miyawaki, S., Rhoads, B., Sukhodolov, A., 2012. An investigation of the dynamics and role played by streamwise oriented vortical cells at stream confluences with a large angle between the incoming streams. J. Geophys. Res.-Earth Surface, under review.

Constantinescu, G., Squires, K.D., 2004. Numerical investigation of the flow over a sphere in the subcritical and supercritical regimes. Phys. Fluids 16, 1449-1467.

Dinehart, R.L., 1992. Evolution of coarse gravel bed forms – field measurements at flood stage. Water Resour. Res. 28, 2667-2689.

Diplas, P., Dancey, C.L., Celik, A.O., Valyrakis, M., Greer, K., Akar, T., 2008. The role of impulse on the initiation of particle movement under turbulent flow conditions. Science 322, 717-720.

Dubief, Y., Delcayre, F., 2000. On coherent-vortex identification in turbulence. J. Turbul. 1, 1-22.

Escauriaza, C., Sotiropoulos, F., 2011. Lagrangian model of bed-load transport in turbulent junction flows. J. Fluid Mech. 666, 36-76.

Ferguson, R.I., Parsons, D.R., Lane, S.N., Hardy, R.J., 2003. Flow in meander bends with recirculation at the inner bank. Water Resour. Res. 39, 1322, doi: 10.1029/2003WR001965.

Frothingham, K.M., Rhoads, B.L., 2003. Three-dimensional flow structure and channel change in an asymmetrical compound meander loop, Embarras River, Illinois. Earth Surf. Proc. Land. 28, 625-644.

Germano, M., 1992. Turbulence: The filtering approach. J. Fluid Mech. 238, 325-336.

Geurts, B.J., 2003. Elements of Direct and Large Eddy Simulation. R. T. Edwards, 344 pp.

Geurts, B.J., Holm, D.D., 2003. Regularization modeling for large-eddy simulation. Phys. Fluids 15, L13-L16.

Hardy, R.J., Lane, S.N., Ferguson, R.I., Parsons, D.R., 2003. Assessing the credibility of a series of computational fluid dynamics simulations of open channel flow. Hydrol. Proc. 17, 1539-1560.

Hardy R.J., Lane, S.N., Lawless, M.R., Best, J.L., Elliott, L., Ingham, D.B., 2005. Development and testing of a numerical code for treatment of complex river channel topography in three-dimensional CFD models with structured grids. J. Hydraul. Res. 43, 468-480.

Hardy, R.J., Lane, S.N., Ferguson, R.I., 2007. Emergence of coherent flow structures over a gravel surface: A numerical experiment. Water Resour. Res. 43, W03422, doi:10.1029/2006WR004936.

Hardy, R.J., Best, J.L., Lane, S.N., Carbonneau, P.E., 2009. Coherent flow structures in a depth-limited flow over a gravel surface: The role of near-bed turbulence and influence of Reynolds number. J. Geophys. Res. 114, F01003, doi: 10.1029/2007JF000970.

Hardy, R.J., Best, J.L., Lane, S.N., Carbonneau, P.E., 2010. Coherent flow structures in a depth-limited flow over a gravel surface: The influence of surface roughness. J. Geophys. Res. 115, F03006, doi:10.1029/2009JF001416.

Heathershaw, A.D., Thorne, P.D., 1985. Sea-bed noises reveal role of turbulent bursting phenomenon in sediment transport by tidal currents. Nature 316, 339-342.

Hunt J.C.R., Abell, C.J., Peterka, J.A., Woo, H., 1978. Kinematic studies of the flow around free or surface mounted obstacles; applying topology to flow visualization. J. Fluid Mech. 86, 179-200.

Julien, P.Y., Anthony, D.J., 2002. Bed load motion and grain sorting in a meandering stream, J. Hydraul. Res. 40, 125-133.

Kenworthy, S.T., Rhoads, B.L., 1995. Hydrologic control of spatial pattern of suspended sediment concentration at a small stream confluence. J. Hydrol. 168, 251-263.

Keylock, C.J. 2010. Characterizing the structure of nonlinear systems using gradual wavelet reconstruction, Nonlinear Proc. Geophys. 17, 615-632.

Keylock, C.J., Hardy, R.J., Parsons, D.R., Ferguson, R.I., Lane, S.N., Richards, K.S., 2005. The theoretical foundations and potential for large-eddy simulation (LES) in fluvial geomorphic and sedimentological research. Earth-Sci. Rev. 71, 271-304.

Keylock, C.J., Tokyay, T.E., Constantinescu, G., 2011. A method for characterising the sensitivity of turbulent flow fields to the structure of inlet turbulence, J. Turbul. 12, N45, doi: 10.1080/14685248.2011.636047

Kirkbride, A.D., 1993. Observations of the influence of bed roughness on turbulence structure in depth-limited flows over gravel beds. In Clifford N.J., French J.R., Hardisty J. (eds). Turbulence: Perspectives on flow and sediment transport. John Wiley and Sons. Chichester.UK. 360pp.

Kirkil, G., Constantinescu, G., 2010. Flow and turbulence structure around an in-stream rectangular cylinder with a scour hole, Water Resour. Res. 46, W11549, doi:10.1029/2010WR009336.

Klaven, A.B., 1966. Investigation of the flow turbulent structure (in Russian) Trans. State Hydrol. Inst. 136, Gidrometeoizdat, Leningrad, Russia, 65–76.

Klaven A.B., Kopaliani, Z.D., 1973. Laboratory investigations of the kinematic structure of turbulent flow over a rough bed (in Russian). Trans. State Hydrol. Inst. 209, Gidrometeoizdat, Leningrad, Russia, pp. 67–90.

Koken, M., Constantinescu, G., 2008a. An investigation of the flow and scour mechanisms around isolated spur dikes in a shallow open channel. Part I. Conditions corresponding to the initiation of the erosion and deposition process. Water Resour. Res. 44, W08406, doi:10.1029/2007WR006489.

Koken, M., Constantinescu, G., 2008b. An investigation of the flow and scour mechanisms around isolated spur dikes in a shallow open channel. Part II. Conditions corresponding to the final stages of the erosion and deposition process. Water Resour. Res. 44, W08407, doi:10.1029/2007WR006491.

Komar, P.D., Li, Z., 1986. Pivoting analyses of the selective entrainment of sediments by shape and size with application to gravel threshold. Sedimentology 33, 425-436.

Lane, S.N., Bradbrook, K.F., Richards, K.S., Biron, P.A., Roy, A.G., 1999. The application of computational fluid dynamics to natural river channels: three-dimensional versus two-dimensional approaches. Geomorphology 29, 1-20.

Lane S.N., Hardy, R.J., Elliott, L., Ingham, D.B., 2002. High resolution numerical modelling of three-dimensional flows over complex river bed topography. Hydrol. Proc. 16, 2261-2272.

Lane S.N., Hardy, R.J., Elliott, L., Ingham, D.B., 2004. Numerical modelling of flow processes over gravelly-surfaces using structured grids and a numerical porosity treatment. Water Resour. Res. 40, WO1302, doi:10.1029/2002WR001934.

Launder B.E., Reece G.J., Rodi W., 1975. Progress in the development of a Reynolds- stress turbulence closure. J. Fluid Mech. 68, 537-566.

Lawless, M., Robert, A., 2001. Three-dimensional flow structure around small-scale bedforms in a simulated gravel-bed environment. Earth Surf. Proc. Land. 26, 507-522.

Leeder, M. R., Bridges, P. H., 1975. Flow separation in meander bends. Nature 253, 338-339.

Lien, F.S., Leschziner, M.A., 1994. Assessment of turbulence-transport models including nonlinear RNG eddy-viscosity formulation and 2nd-moment closure for flow over a backward-facing step. Comp. & Fluids 23, 983-1004.

McCoy, A., Constantinescu, G., Weber, L.J., 2008. Numerical investigation of flow hydrodynamics in a channel with a series of groynes, J. of Hydraul. Eng.-ASCE 134, 157-172.

Moncho-Esteve, I., Palau-Salvador, G., Shiono, K., Muto, Y., 2010. Turbulent structures in the flow through compound meandering channels. Proceeding of River Flow 2010, Eds. Dittrich, Koll, Aberle and Geisenhainer, Braunschweig, Germany, published by Bundesanstalt fur Wasserbau, Karlsruhe, Germany.

Nelson, J.M., Shreve, R.L., McLean, S.R., Drake, T.G., 1995. Role of near-bed turbulence structure in bed load transport and bed form mechanics. Water Resour. Res. 31, 2071-2086.

Niño, Y., García, M., 1996. Experiments on particle-turbulence interactions in the near -wall region of an open channel flow: implications for sediment transport. J. Fluid Mech. 326, 285-319.

Olsen, N.R.B., Stokseth, S., 1995. 3-dimensional numerical modeling of water flow in a river with large bed roughness. J. Hydraul. Res. 33, 571-581.

Paola, C., 1997. When streams collide. Nature 387, 232-233.

Piomelli, U., Balaras, E., 2002. Wall-layer models for Large-Eddy Simulations. Ann. Rev. Fluid Mech. 34, 349-374.

Porté-Agel, F., Meneveau, C., Parlange, M.B., 2000. A scale-dependent dynamic model for large-eddy simulation: application to a neutral atmospheric boundary layer. J. Fluid Mech. 415, 261-284.

Rhoads, B.L., Sukhodolov, A.N., 2001. Field investigation of three-dimensional flow structure at stream confluences: Part I. Thermal mixing and time-averaged velocities, Water Resour. Res. 37, 2393-2410.

Rhoads, B.L., Sukhodolov, A.N., 2008. Lateral momentum flux and the spatial evolution of flow within a confluence mixing interface, Water Resour. Res. 44, W08440, doi:10.1029/2007WR006634.

Robert A., Roy, A.G., De Serres, B., 1993. Space-time correlations of velocity measurements at a roughness transition in a gravel-bed river. In Clifford N.J., French J.R., Hardisty J. (eds). Turbulence: Perspectives on flow and sediment transport. John Wiley and Sons. Chichester.UK. 360pp.

Roy A.G., Buffin-Belanger, T., Deland, S., 1996. Scales of turbulent coherent structures in a Gravel-bed River. In Ashworth, P.J., Bennett, S.J., Best, J.L., and McLelland, S.J., Coherent Flow Structures in Open Channels, John Wiley and Sons, Chichester.

Rumsey, C.L., 2007. Apparent transition behavior of widely-used turbulence models. Int. J. Heat Fluid Flow 28, 1460-1471.

Sagaut, P., 2005. Large Eddy Simulation for Incompressible Flows, 3rd ed., Springer, 556 pp.

Schmeeckle, M.W., Nelson, J.M., Shreve, R.L. 2004. Forces on stationary particles in near-bed turbulent flows. J. Geophys. Res. 112, F02003, doi: 10.1029/2006JF000536.

Schnauder, I., Sukhodolov, A.N., 2012. Flow in a tightly curving meander bend: effects of seasonal changes in aquatic macrophyte cover. Earth Surf. Proc. Land. early-view. doi: 10.1002/esp.3234.

Shvidchenko, A., Pender, G., 2001. Macroturbulent structure of open-channel flow over gravely beds. Water Resour. Res. 37, 709-719.

Simpson, R.L., 1989. Turbulent boundary-layer separation. Ann. Rev. Fluid Mech. 21, 205-234.

Smagorinsky, J., 1963. General circulation experiments with the primitive equations. Part I: The basic experiment. Month. Weath. Rev. 91, 99-167.

Spalart, P. R., 2000. Strategies for turbulence modelling and simulations, Int. J. Heat Fluid Flow 21, 252-263.

Spalart, P.R., Allmaras, S.R., 1994. A one-equation turbulence model for aerodynamic flows. Recherche Aerospat. 1, 5-21.

Speziale, C.G., 1987. On nonlinear K-l and K-ε models of turbulence. J. Fluid Mech. 178, 459-475.

Sukhodolov, A.N. 2012. Structure of turbulent flow in a meander bend in a lowland river, Water Resour. Res. 48, W01516, doi: 10.1029/2011WR010765.

Sukhodolov, A.N., Rhoads, B.L., 2001. Field investigation of three-dimensional flow structure at stream confluences: Part II. Turbulence, Water Resour. Res. 37, 2411-2424.

Sukhodolov, A.N., Schanuder, I., Uijttewaal, W.S.J., 2010. Dynamics of shallow lateral shear layers: Experimental study in a river with a sandy bed, Water Resour. Res. 46, W11519, doi:10.1029/2010WR009245.

Tabor, G., Baba-Ahmadi, M.H., 2010. Inlet conditions for large eddy simulations: A review. Comp. & Fluids 39, 553–567.

Tonina, D., Buffington, J.M., 2011. Effects of stream discharge, alluvial depth and bar amplitude on hyporheic flow in pool-riffle channels. Water Resour. Res. 47, W08508, doi: 10.1029/2010WR009140.

van Balen, W., Blanckaert, K., Uijttewaal W.S.J., 2010a. Analysis of the role of turbulence in curved open-channel flow at different water depths by means of experiments, LES and RANS. J. Turbul. 11, 12, 1-34.

van Balen, W., Uijttewaal, W.S.J., Blanckaert, K., 2010b. Large-eddy simulation of a curved open-channel flow over topography. Phys. Fluids 22, 075108, doi: 10.1063/1.3459152.

Valyrakis, M., Diplas, P., Dancey, C.L., Greer, K., Celik, A.O. 2010. The role of instantaneous force magnitude and duration on particle entrainment. J. Geophys. Res. 115, F02006, doi:10.1029/2008JF001247.

Vreman, B., Geurts, B., Kuerten, H., 1994. Realizability conditions for the turbulent stress tensor in large eddy simulation. J. Fluid Mech. 278, 351-362.

Wang, M., Moin, P., 2002. Dynamic wall modeling for large eddy simulation of complex turbulent flows. Phys. Fluids 14, 2043-2051.

Wiberg, P.L., Smith, J.D., 1991. Velocity distribution and bed roughness in high gradient streams. Water Resour. Res. 27, 825-838.

Wiberg, P.L., Smith, J.D., 1985. A theoretical model for saltating grains in water. J. Geophys. Res. 90, 7341-7354.

Wilcock, P.R., 1993. Critical shear stress of natural sediments. J. Hydraul. Eng.–ASCE 119, 491-505.

Zeng, J., Constantinescu, G., Blanc, K., Weber, L., 2008. Flow and bathymetry in sharp open-channel bends: Experiments and predictions. Water Resour. Res. 44, W09401, doi:10.1029/2007WR006303.

List of Figures.

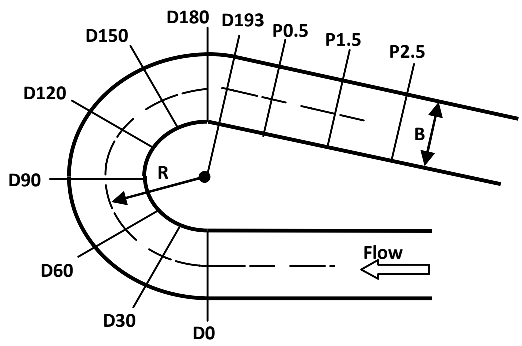

Figure 1. Sketch of flume in which the 193^0 bend experiments with flat bed and with deformed mobile bed (Blanckaert, 2010) were conducted. The prefix "D" indicates measured cross-sections on the bend (with their angular distance around the bend also given). The prefix "P" indicates the post-bend cross-sections (with their distance in meters stated).

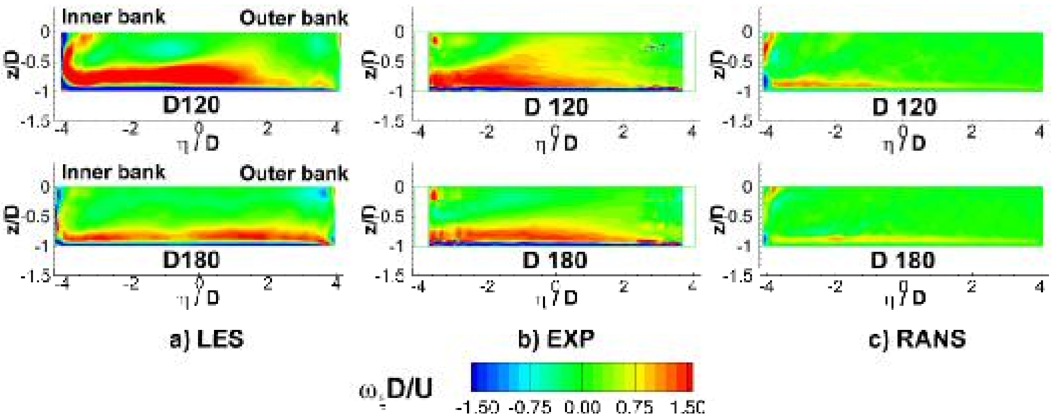

Figure 2. Distribution of streamwise vorticity, $\omega_\xi D/U$, in sections D120 and D180 (as shown in Fig. 1) for the flat bed case. a) LES (left); b) experiment (middle); c) RANS (right).

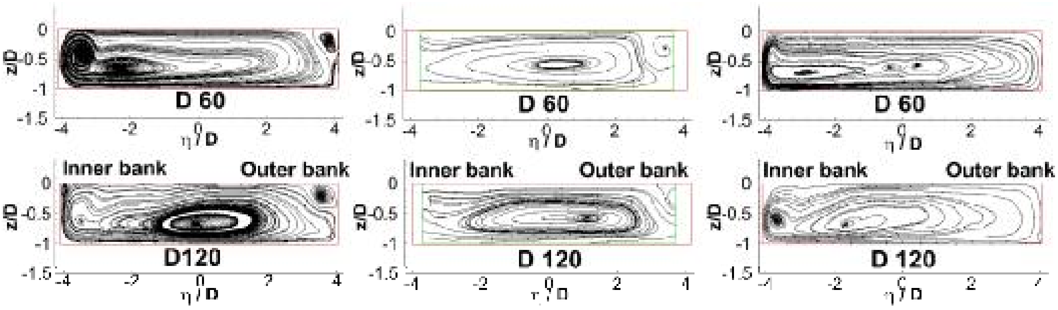

Figure 3. Distribution of 2-D streamline patterns in sections D60 and D120 (see Fig. 1) for the flat bed case. a) LES (left); b) experiment (middle); c) RANS (right).

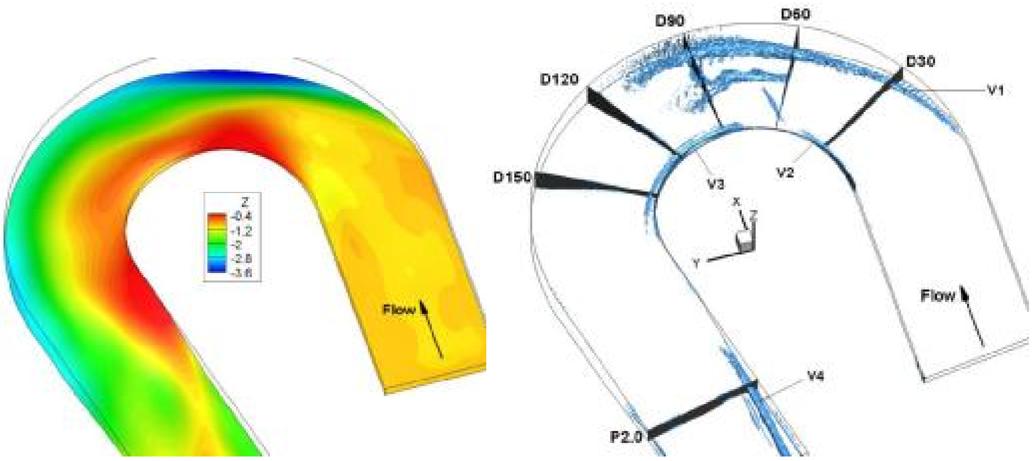

Figure 4. Equilibrium bathymetry (left) and vortical structure of the mean flow predicted by DES in the deformed bed case (right). The bed elevation (*z/D*) is measured with respect to the mean position of the free surface (*z/D* = 0) in the inlet section. The vortices are visualized using the *Q* criterion.

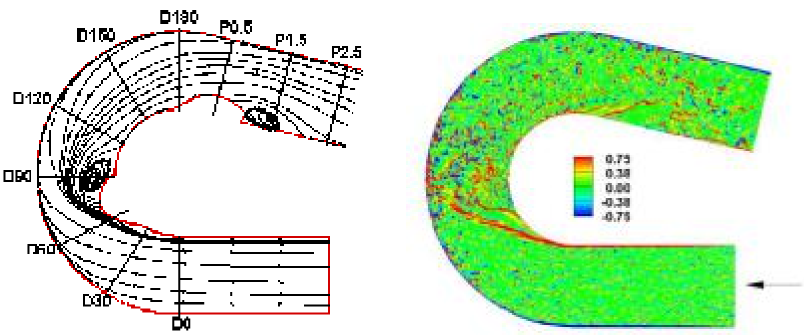

Figure 5. 2-D mean-flow streamlines patterns in a horizontal section situated at *z/D* = -0.5 (left) and vertical vorticity, ω_ξ *D/U*, at the free surface (*z/D* = 0) in one of the instantaneous flow fields (right) for the deformed bed case. The figure is from: Constantinescu, G., Koken, M., Zeng, J., 2011. The structure of turbulent flow in an open channel bend of strong curvature with deformed bed: Insight provided by detached eddy simulation. Water Resources Research 47, W05515, doi:10.1029/2010WR010114, copyright (2011) American Geophysical Union. Figure is reproduced by permission of the American Geophysical Union.

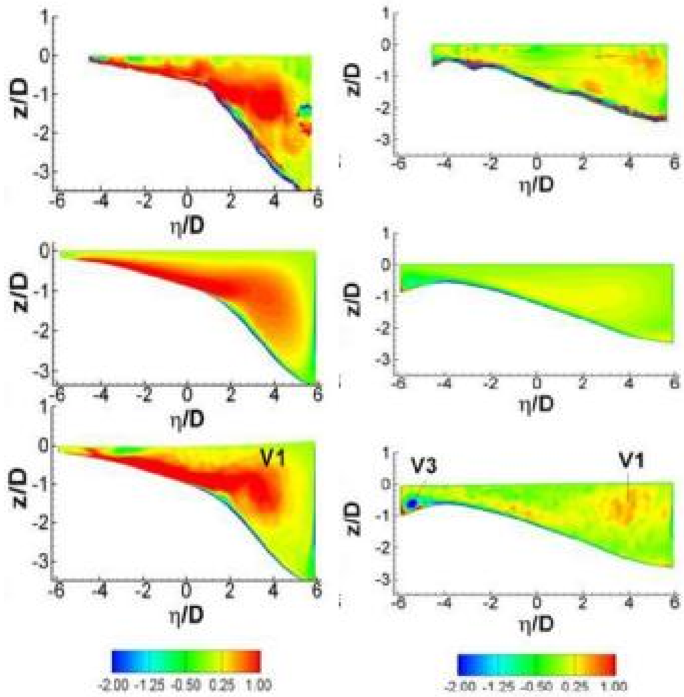

Figure 6. Streamwise vorticity, $\omega_{\xi} D/U$ in sections D60 (left) and D120 (right) obtained from experiment (top), RANS (middle) and DES (bottom) for the deformed bed case. The figure is from: Constantinescu, G., Koken, M., Zeng, J., 2011. The structure of turbulent flow in an open channel bend of strong curvature with deformed bed: Insight provided by detached eddy simulation. Water Resources Research 47, W05515, doi:10.1029/2010WR010114, copyright (2011) American Geophysical Union. Figure is reproduced by permission of the American Geophysical Union.

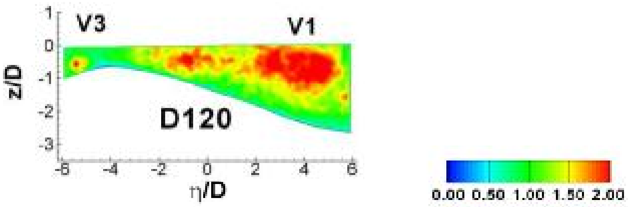

Figure 7 Turbulent kinetic energy, $100k/U^2$, in section D120 for the deformed bed case. The figure is from: Constantinescu, G., Koken, M., Zeng, J., 2011. The structure of turbulent flow in an open channel bend of strong curvature with deformed bed: Insight provided by detached eddy simulation. Water Resources Research 47, W05515, doi:10.1029/2010WR010114, copyright (2011) American Geophysical Union. Figure is reproduced by permission of the American Geophysical Union.

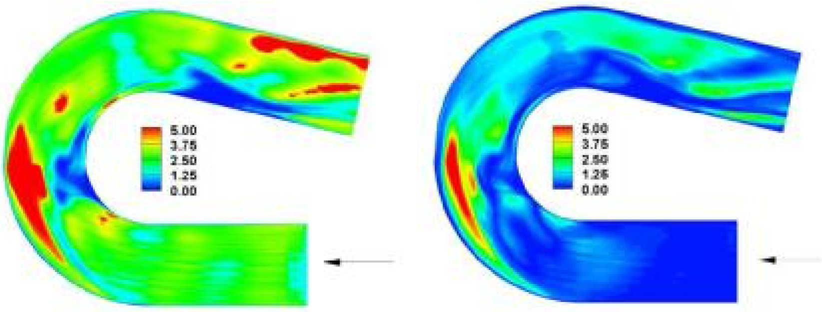

Figure 8. Magnitude (left) and transverse component (right) of the nondimensional shear stress at the bed, τ / τ_0, estimated for the deformed bed case. The figure is from: Constantinescu, G., Koken, M., Zeng, J., 2011. The structure of turbulent flow in an open channel bend of strong curvature with deformed bed: Insight provided by detached eddy simulation. Water Resources Research 47, W05515, doi:10.1029/2010WR010114, copyright (2011) American Geophysical Union. Figure is reproduced by permission of the American Geophysical Union.

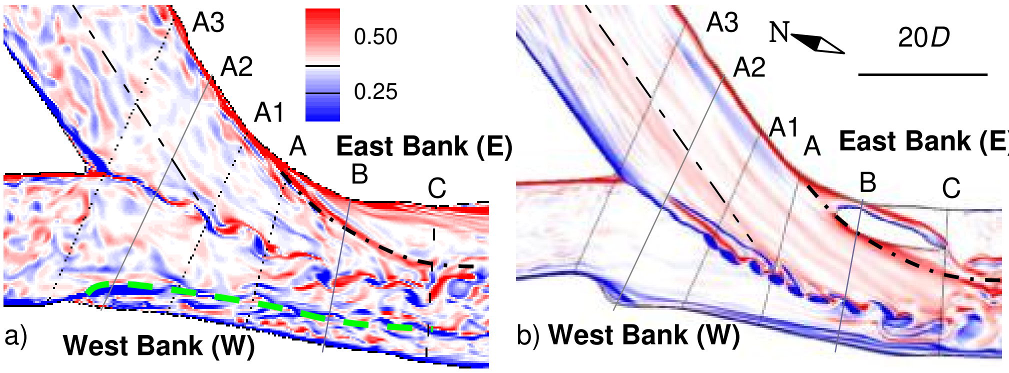

Figure 9 Distribution of the vertical vorticity, $\omega_z D/U$, in the instantaneous flow in a horizontal surface situated 0.1D below the free surface. a) Case 1; b) Case 2. The black dashed line follows the centerline of the Copper Slough (CS) stream until it intersects the MI (from Constantinescu et al., 2012). Vorticity values are dimensionless.

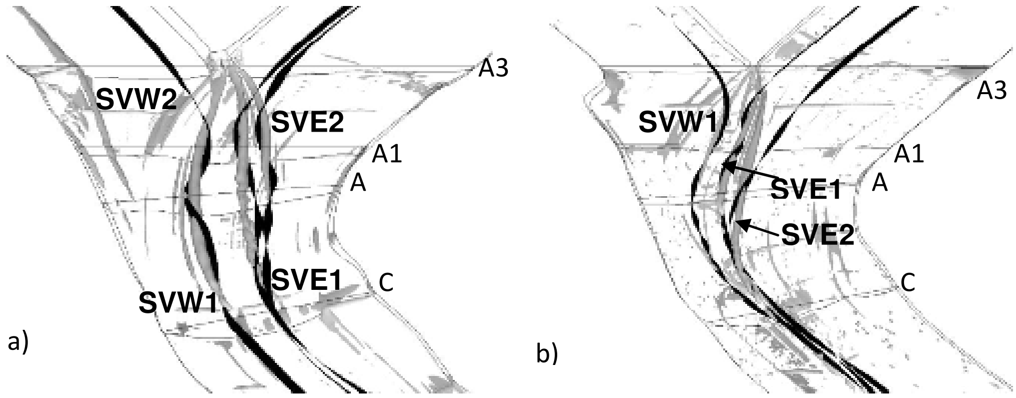

Figure 10 Visualization of the main vortical structures in the mean flow using a Q iso-surface. a) Case 1; b) Case 2. The 3-D ribbons visualize the helical motion of the particles inside the SOV cells (from Constantinescu et al., 2012).

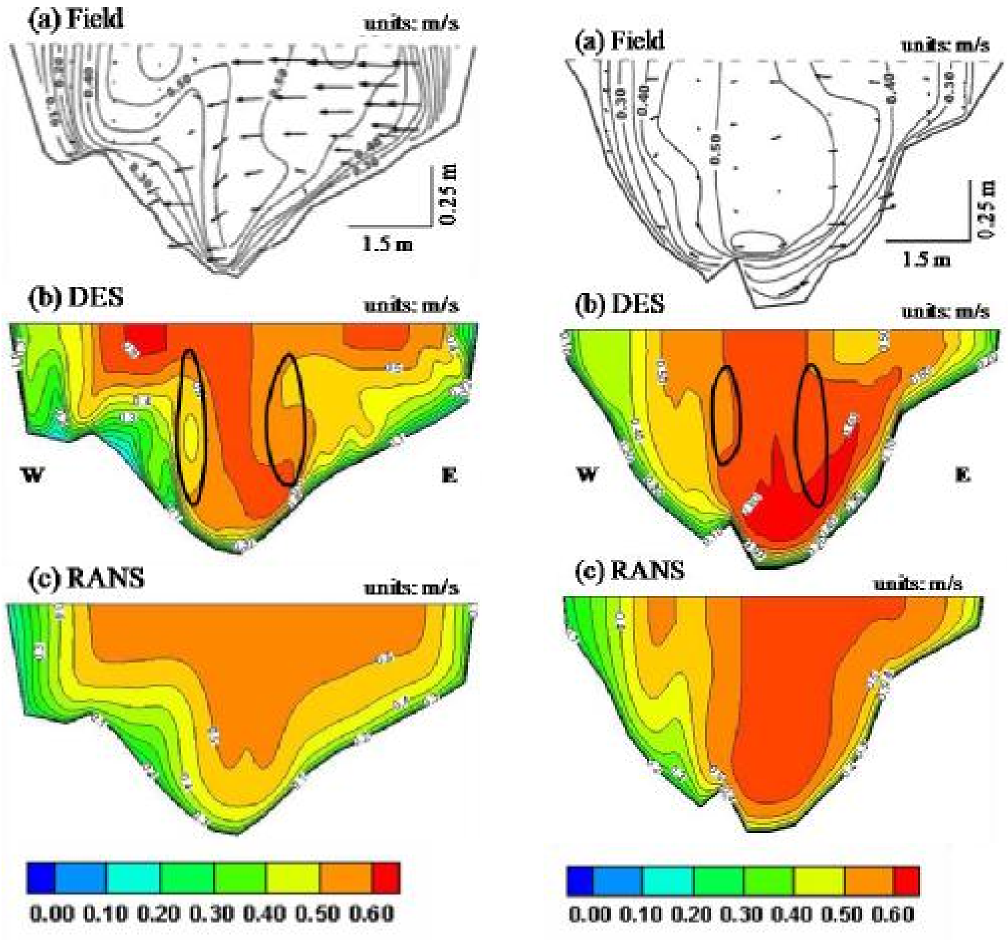

Section A **Section C**

Figure 11. Distribution of the mean streamwise velocity, u_s (units for contours and the scale bar are ms^{-1}), in section A (left) and section C (right) for Case 1. a) field experiment; b) DES; c) RANS. The scale is distorted in the vertical direction (aspect ratio is 1:0.208). The solid lines visualize the position of the main SOV cells in the cross section. The figure is from: Constantinescu, G., Miyawaki, S., Rhoads, B., Sukhodolov, A., Kirkil, G., 2011. Structure of turbulent flow at a river confluence with momentum and velocity ratios close to 1: Insight provided by an eddy-resolving numerical simulation. Water Resources Research 47, W05507, doi: 10.1029/2010WR010018, copyright (2011) American Geophysical Union. Figure is reproduced by permission of the American Geophysical Union.

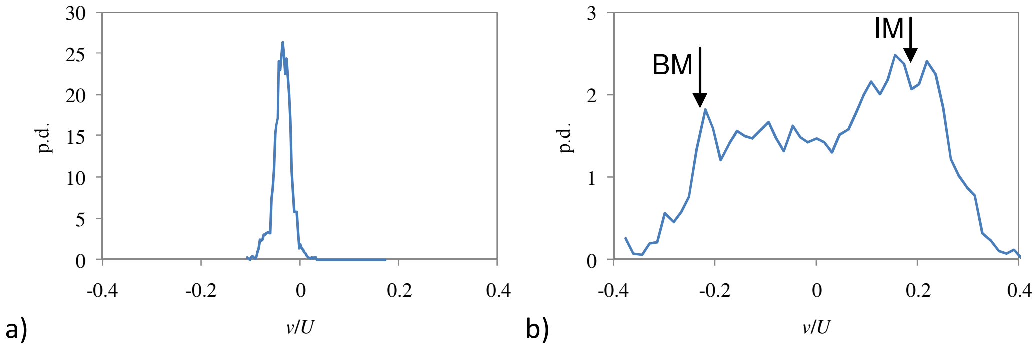

Figure 12 Probability-density function of the vertical component of the instantaneous velocity, *v/U*, for Case 1 at two points situated in section A1. a) within the mixing interface; b) close to the axis of SVE1 in the mean flow. IM and BM denote the interface mode and the bank mode, respectively (from Constantinescu et al., 2012).

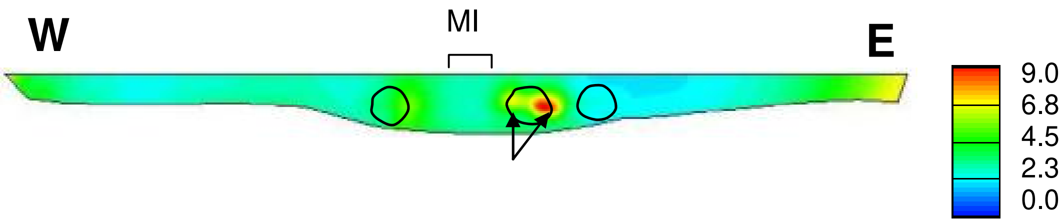

Figure 13. Distribution of the mean pressure fluctuations, $\overline{p'^2} / \rho^2 U^4$ (×10^3), at section A1 for Case 1. The *Q* criterion is used to visualize the cores of the SOV cells in the mean flow (see also Figure 10a). The arrows point toward the location of the two pressure peaks observed in the region where the core of SVE1 is subject to bimodal oscillations (from Constantinescu et al., 2012).

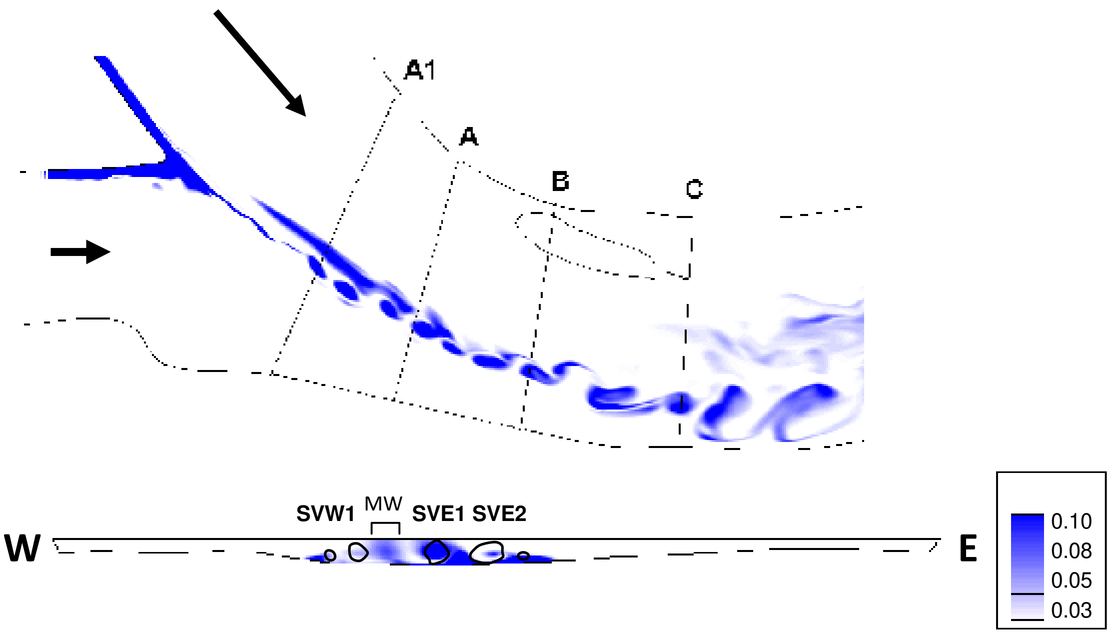

Figure 14. Instantaneous distribution of the concentration of a passive scalar introduced around the junction corner for Case 2: a) horizontal surface situated 0.1*D* below the free surface; b) section A1 (from Constantinescu et al., 2012).

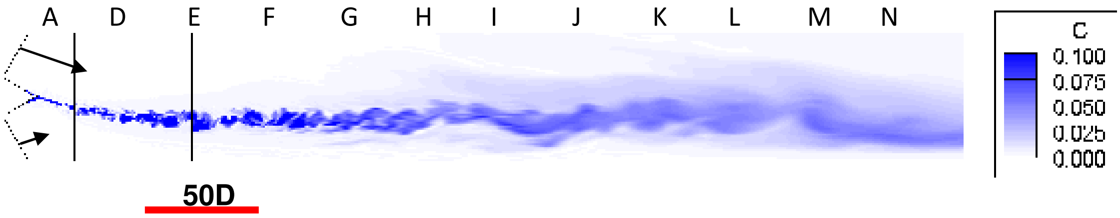

Figure 15 Visualization of the instantaneous structure of the mixing interface at the confluence of two wide streams making an angle of 60^0 in a flat bed channel of constant depth, D. The momentum ratio is equal to 2 and the Reynolds number in the main channel is Re=200 000. A passive scalar with C=1 is introduced around the junction corner. The concentration field is shown at the free surface.

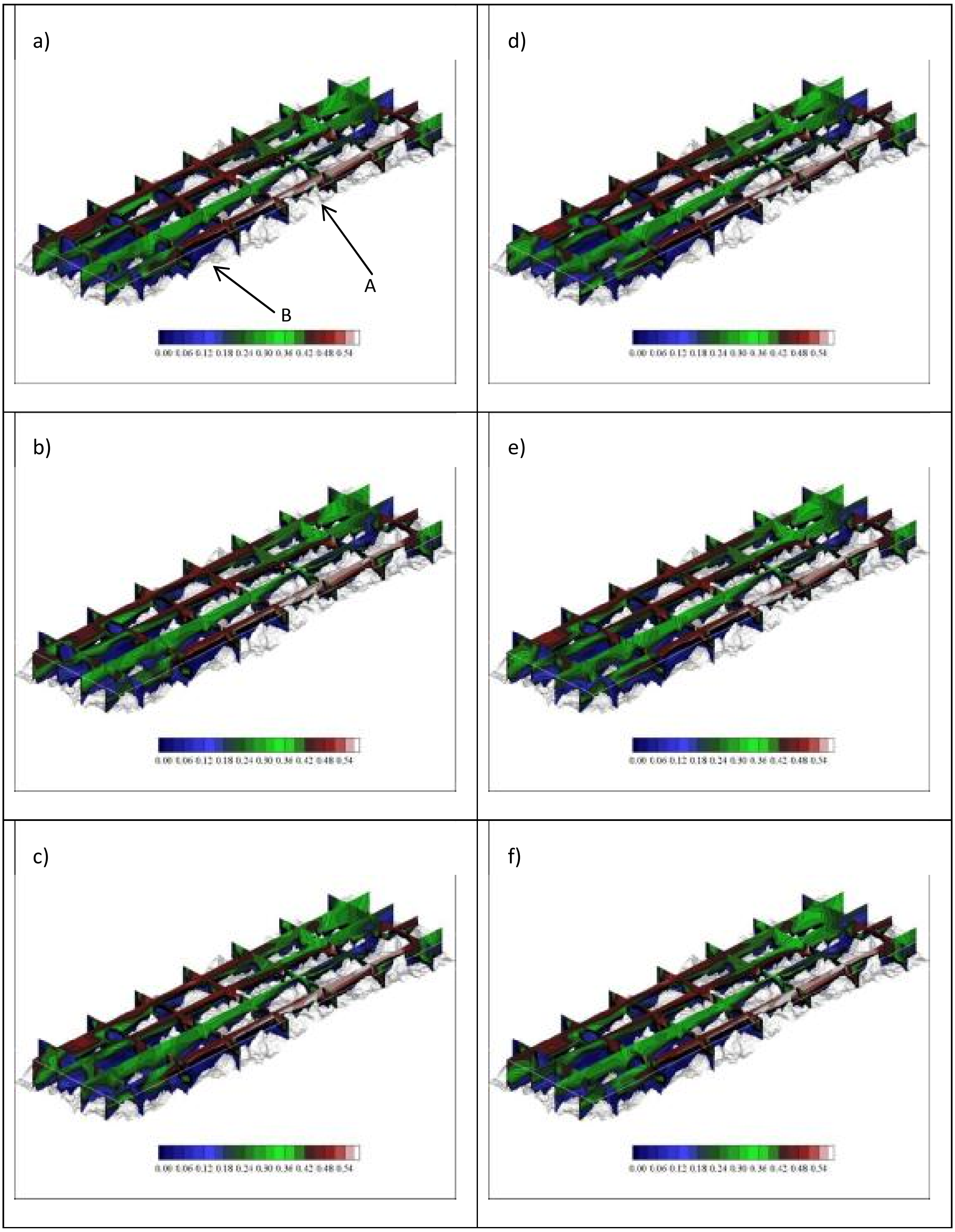

Figure 16. An example of time dependent flow predicted by LES over a gravel surface. The gravel DEM is represented with the grey surface on a 0.002 m resolution. The colour slices represent the velocity magnitude, the resolved component of the *u*-, *v*- & *w*- velocity, where each image is 1 second apart.

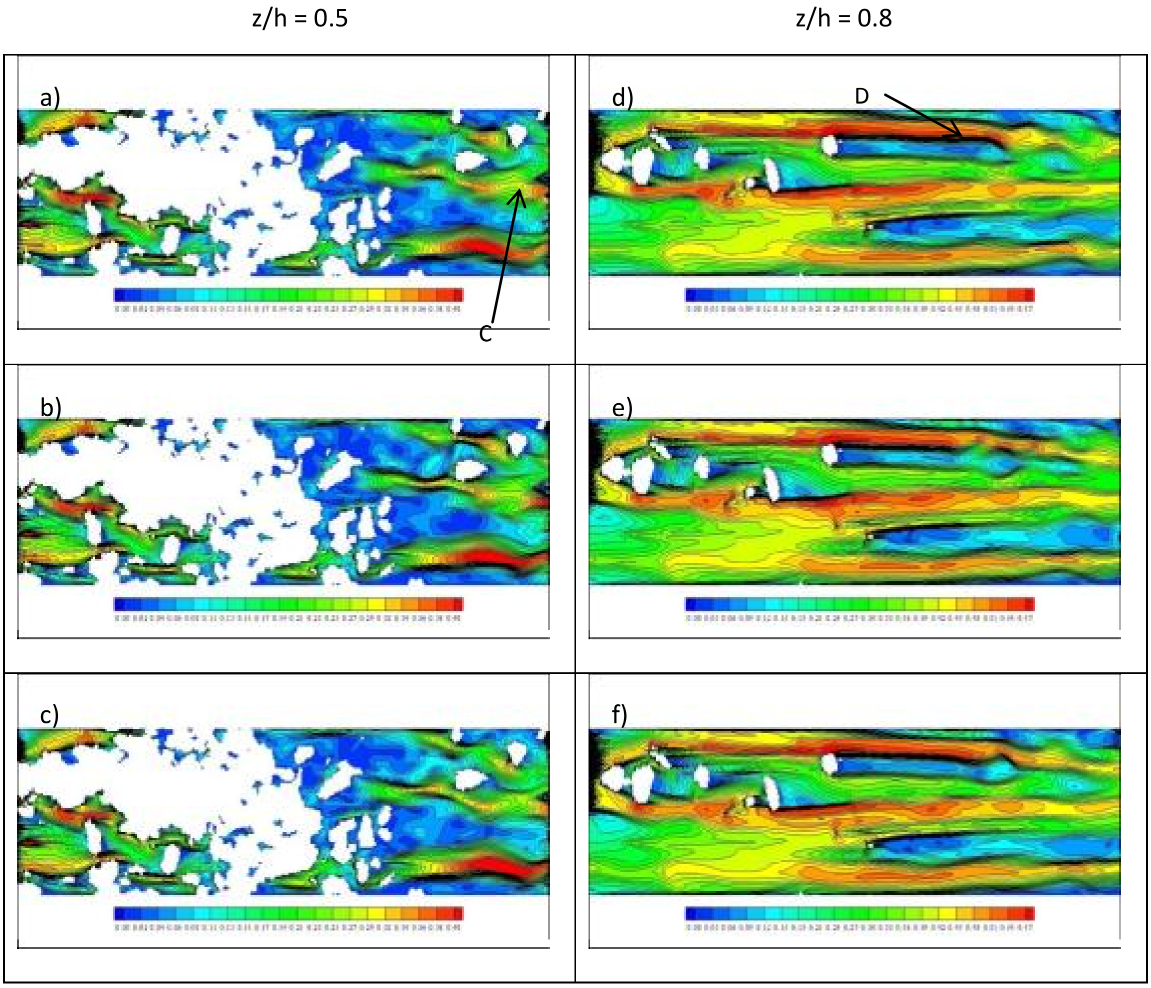

Figure 17. A time series of plan views of velocity magnitudes for *z/h* = 0.5 (a-c) and *z/h* = 0.8 (d-f). Flow is from left to right. White regions represent areas blocked out with the mass flux scaling algorithm.

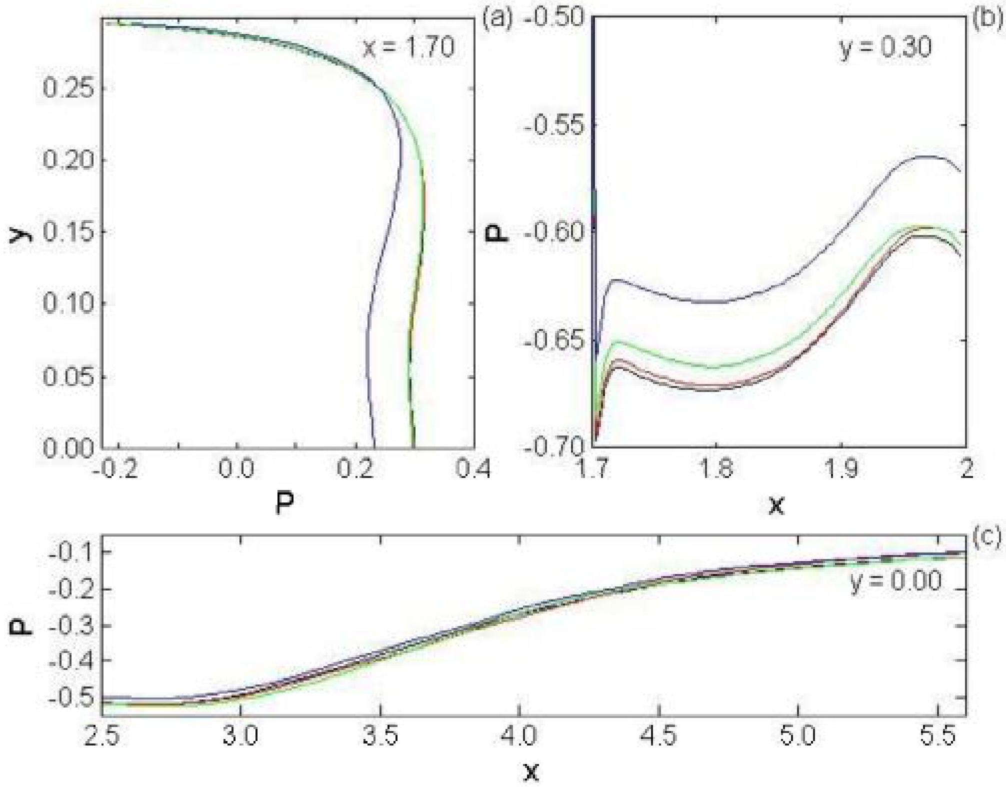

Figure 18. Profiles of the time-averaged pressure field, *P*, for well-resolved LES of the flow over a wall-mounted square rib considered by Keylock et al. (2011). Shown are the vertical profile of mean pressure on the front face of the rib (a), the pressure on the top surface of the rib (b), and the pressure at the wall in the region downstream of the rib and close to reattachment (x = 4.5). The various lines are for simulations degraded to varying degrees depending on the value for a threshold parameter, ρ_{thresh}, as described in the text. The blue, green, red, and black lines are for ρ_{thresh} = 0.0, 0.65, 0.9 and 1.0, respectively. Figure is taken from: Keylock, C.J., Tokyay, T.E., Constantinescu, G., 2011. A method for characterising the sensitivity of turbulent flow fields to the structure of inlet turbulence, Journal of Turbulence 12, N45, doi: 10.1080/14685248.2011.636047 and is reproduced by permission of the publisher (Taylor & Francis Ltd).